Utah State University

DigitalCommons@USU

All Graduate Theses and Dissertations | Graduate Studies

5-2008

Algorithm Development of the Aglite-Lidar Instrument

Christian Marchant
Utah State University

Follow this and additional works at: https://digitalcommons.usu.edu/etd

 Part of the Electrical and Electronics Commons, Environmental Engineering Commons, and the Optics Commons

Recommended Citation

Marchant, Christian, "Algorithm Development of the Aglite-Lidar Instrument" (2008). *All Graduate Theses and Dissertations*. 107.
https://digitalcommons.usu.edu/etd/107

This Thesis is brought to you for free and open access by the Graduate Studies at DigitalCommons@USU. It has been accepted for inclusion in All Graduate Theses and Dissertations by an authorized administrator of DigitalCommons@USU. For more information, please contact digitalcommons@usu.edu.

ALGORITHM DEVELOPMENT OF THE AGLITE-LIDAR INSTRUMENT

by

Christian C. Marchant

A thesis submitted in partial fulfillment
of the requirements for the degree

of

MASTER OF SCIENCE

in

Electrical Engineering

Approved:

_____	_____
Dr. Charles Swenson Major Professor	Dr. Vladimir Zavyalov Committee Member
_____	_____
Dr. Todd Moon Committee Member	Dr. Byron Burnham Dean of Graduate Studies

UTAH STATE UNIVERSITY
Logan, Utah

2008

Copyright © Christian C. Marchant 2008

All Rights Reserved

ABSTRACT

Algorithm Development of the Aglite-Lidar Instrument

by

Christian C. Marchant, Master of Science

Utah State University, 2008

Major Professor: Dr. Charles Swenson
Department: Electrical and Computer Engineering

Particulate emissions from agricultural operations are increasingly receiving attention from regulatory bodies as a potential source of air pollution. The Space Dynamics Laboratory (SDL) has developed the Aglite system, a suite of instruments including a lidar that is capable of measuring particulate emission levels from agricultural facilities. This system provides a novel method of measuring particulate mass (PM) pollution, allowing measurements to be taken of diverse types of facilities with high temporal and spatial resolution. This high resolution allows for the measurement of emission levels generated by specific activities, fostering the development and determination of best management practices.

The Aglite system consists of a mobile scanning multi-wavelength lidar, together with a set of conventional instruments. The lidar performs 3D scans of the air surrounding the facility. The lidar maps the concentration of particulates in the

atmosphere surrounding the facility with high spatial and temporal resolution. Data from the conventional instruments are used to calibrate the lidar.

The design of the Aglite lidar can be divided into three categories: the hardware, the optics, and the software. The software subsystem includes the lidar control software and the lidar retrieval program. The lidar retrieval program combines the data from the lidar instrument with data from the conventional instruments to produce measurements of particulate concentration values. The high spatial and temporal resolution of the data produced by this software enables the radical capabilities of the Aglite system to measure total facility emissions and to correlate emission rates with specific agricultural practices.

This thesis describes the design of the lidar data retrieval program, the development and implementation of the algorithm, and the results of measurements made on the initial field campaign. This document is divided into four chapters. The first chapter describes the background of agricultural air pollution and the methodology used by the Aglite system in performing measurements. The second chapter describes the lidar retrieval program and the details of the algorithm. The third chapter presents the results of the measurements made by the instrument on its first field campaign. The final chapter discusses the performance of the instrument and future areas of research for the improvement of the algorithm.

(73 pages)

ACKNOWLEDGMENTS

I would like to state my gratitude to those who have made this thesis possible. I am grateful to all my friends, family, and colleagues who have supported me in my education and specifically in this thesis.

I would like to thank the faculty of the Electrical and Computer Engineering department. In particular, I would like to recognize Dr. Jacob Gunther and my committee members, Drs. Charles Swenson and Todd Moon. They provided much valuable advice in the completion of both the research and thesis.

The Aglite project has been a phenomenal success, due to the hard work and skill of its team members. Inasmuch as this thesis is a direct product of that success, I would like to acknowledge the entire Aglite team, both full-time engineers and students, and all who contributed to it.

In particular I would like to recognize Jason Swasey for his outstanding systems engineering work and his endless patience in coordinating the several needs and requirements of the project. I am grateful to Vladimir Zavyalov, my mentor and committee member, who has provided guidance and support in understanding the principles of lidar retrieval. I would like to acknowledge Gail Bingham, the principal investigator of the Aglite project. I would also like to acknowledge Tom Wilkerson for his advice in this area and for his leadership on this project.

I would also like to recognize the work performed by the many students who have directly assisted me on the research for this thesis, including Christopher Rogers, Timothy Turpin, Douglas Ahlstrom, Paul Timothy, and Tanner Jones. I need to recognize

Scott Cornelsen, who did a superb job designing the system electronics.

Finally, I would be remiss if I did not thank my family, and in particular my loving wife, for their encouragement and support. Without them, this thesis would not have been possible. My parents have provided me with valuable advice and support, and I am so grateful for my wonderful wife, Hanna. I am entirely dependent on her support and patience.

Christian Marchant

CONTENTS

Page

LIST OF FIGURES

CHAPTER 1

INTRODUCTION

A. *Project Background and Relevance*

The contribution to air pollution by agricultural operations is a growing concern for surrounding society. The US Environmental Protection Agency (EPA) is currently investigating the impact of agricultural operations as sources of pollution. These facilities can potentially generate pollutants that impact both the environment and human health. Measurements of emissions from agricultural operations are necessary for determining the contribution to air pollution by these facilities and also for determining the efficacy of pollution mitigation techniques.

Agricultural operations produce a variety of particulates and gases that influence ambient air quality and are impact the well-being of humans, animals, and plants. Particulates are generated by many types of sources, including animal activities, agricultural operations, and by the interaction of gases to produce fine particles. Although there is a lot of data describing ammonia emissions, the body of literature and corresponding data describing the particulate emission rates of agricultural sources is limited. It is important to know the characteristics of these emissions in order to analyze the impact of agricultural operations on the environment and on human health and quality of life. Essential characteristics include the rate of emission, the emission constituents, and the spatial distribution of the emissions.

Concentrated Animal Feeding Operations (CAFO) in particular are being investigated as a source of air pollutants. The US Department of Agriculture (USDA)

Agriculture Research Service (ARS) has joined with the EPA to develop a program to characterize these emissions and measure the pollutants being emitted from CAFO facilities as well as other agricultural facilities and activities.

The EPA regulations of CAFO emissions are based on point-source pollution measurements taken near these facilities. These sensors are the result of years of testing and integration and are regulated by strict protocols. The conventional technique for measuring agricultural pollution uses these point sensors and software modeling to predict the pollution of a facility [1]. A relatively small number of point sensors are placed around the facility, and data from these instruments are used to calibrate the software model, which estimates the emission rate. Measurements made using these techniques can be imprecise because the emission plume may not always hit the sensor, therefore large time intervals are required for acceptable data. In addition, these measurements can be inaccurate due to inadequacies of the computer model and the small number of instrument measurements.

Agricultural sources vary both temporally and spatially due to daily and seasonal activities and the complex structure of a facility. Additionally, the models used for calculating emissions were developed for large scale regional estimates and can break down under small scale conditions. Variations in environmental conditions and pollutant transport activities make it practically and economically infeasible to monitor actual pollutant source strength using point sensors. It is challenging to adequately determine the spatial and temporal distribution of pollutant emission over these distributed sources using localized point measurements.

Lidar (Light Detection and Ranging) technology provides a means to derive

quantitative information of particulate spatial distribution from remote distances using a single instrument located at convenient point. The lidar can scan the atmosphere around a facility, mapping the concentration of emissions. The Aglite lidar has a spatial resolution of 6 m, and can effectively make up to 10 measurements per second. The lidar has an minimum scanning range from 500 m and can extend to several kilometers. The instrument is capable of scanning an area several hundred meters square in less than a minute. This large sampling rate allows the lidar to make many measurements over a relatively large area in a short amount of time. Additionally, the high temporal resolution allows for the correlation of emission rates with specific events and activities on the site.

The determination of pollution regulations and best management practices requires the ability to make accurate pollution measurements. The correlation of emission rates with management practices determines the efficacy of a practice. In addition, accurate real-time measurements of emissions are needed in order to distinguish the emissions caused by various agricultural practices and to compare the efficacy of specific pollution mitigation techniques. The ability of the Aglite system to correlate emission levels with activities and events on the facility enables the determination of best management practices.

Lidar systems for measuring the atmosphere have been in use since the 1970s. Most are used on fixed slant or vertical paths for mapping the properties of different layers of the atmosphere. Lidar systems have also been used to measure temperature and density profiles of the atmosphere [2]. Other systems have been used to map aerosol boundary layers and determine the constituency and size distribution of these aerosols [3]. More recently, scanning lidar systems have been used to map the spatial anatomy, as

well as composition and particle size distribution, of aerosol plumes near the ground [4-5]. Lidar has also begun to be used to map emissions from agricultural operations [6]. The Aglite lidar is used to extrapolate the anatomy, composition, and total emission rate of aerosol plumes generated by agricultural operations between the fixed-point measurements.

The Aglite system consists of a mobile scanning three-wavelength lidar located more than 500 m from the target facility, combined with point measurements taken by in situ instruments near the facility. Measurements from these conventional in situ instruments such as particle mass samplers and optical particle counters are combined with lidar data to calculate whole facility emissions. The system is capable of measuring the spatial distribution and temporal variability of aerosol emissions and is also able to determine the particle size distribution of the pollutant.

The Aglite lidar can directly measure particulate concentration and particle size distribution with high spatial and temporal resolution over large areas, and thus allows for accurate calculation of total aerosol emissions with fine temporal resolution.

B. *Lidar Instrument*

The Aglite system consists of a lidar mounted in a small trailer, a suite of conventional instruments with a trailer for storage and transport, as well as other equipment including mobile aluminum towers. The Aglite system is designed to be mobile; the instruments and equipment can be deployed to any site of interest.

In addition to the lidar, a set of conventional instruments are used in the Aglite system. Several model 9722 MetOne Optical Particle Counters (OPC) are typically

distributed around the site of interest. These OPC instruments measure the concentration of particles in the atmosphere with the ability to discriminate particles by size. They are able to size particles from 0.3 μm and up into one of eight size bins, with sample reporting every 20 seconds. They have been fitted with transmitters, solar panels, and batteries. This means that data can be retrieved in real time from the instruments, which can be placed at selected locations.

Several portable AirMetrics MiniVol PM filter-based instruments with a range of aerosol size separation heads are also distributed around the facility, usually paired with an OPC instrument, to provide long term source averaging and particulate physical information. Each PM sampler is equipped with either a PM_1, $PM_{2.5}$, PM_{10}, or PM_{TSP} head. An Aerodyne Aerosol Mass Spectrometer (AMS) is housed in the conventional instruments trailer. The AMS instrument is capable of discriminating particles by both size and chemical composition. Meteorological data is collected using a VantagePro 2 weather system from Davis Instruments, Inc. In addition, tower mounted 3D sonic anemometers provide fast response wind speed and direction information for eddy flux and dispersion calculations.

The lidar itself is permanently housed in a small trailer for ease of portability. The trailer contains the optical and control units of the lidar, an air regulation system, and computers for processing the lidar returns.

Lidar operates by emitting a short coherent pulse of light. As the pulse travels through the atmosphere, it is scattered by air molecules and suspended particulate matter. Some of the scattered photons are reflected back to the lidar receiving optics. The detector electronics measure the time delay between when the pulse was emitted and

when a photon is measured. The time delay between the emission of the pulse and the detection of the photons is used to calculate the range at which the scattering occurred.

The optical unit consists of a receiver telescope, an optical bench, and a pointing turret. The optical bench contains the detector electronics, the laser, and transmission and detection optics. The pointing turret is mounted over the telescope. The entire optical unit is mounted on a lift that, during operation, elevates the pointing turret through a hatch in the roof of the trailer. During operation, the pointing turret sits over the roof of the trailer and directs the lidar beam in whatever pattern is required for the experiment. The scanning mirror allows ranges of 0° to 45° for elevation and ±135° for azimuth.

The optical system of the Aglite consists of a laser and transmission optics, combined with a receiver telescope and receiver optics. The transmission and receiver systems are coaxially aligned. The laser of the Aglite lidar is a three-wavelength 6 Watt Nd:YAG laser. It emits on channels with wavelength values of 0.355 μm, 0.532 μm, and 1.064 μm, with a pulse repetition rate of 10 kHz. For convenience, these channels are here labeled ultraviolet (UV), visible (V), and infra-red (IR).

A conceptual diagram of the Aglite lidar is shown in fig. 1.1, and a general description of the Aglite optics is shown by fig. 1.2. The output beam passes through a beam expander and a neutral-density filter (NDF) before moving on to the rest of the transmission optics. For the measurements discussed in this study, the NDF reduces the output power of the lidar by 90%. This was necessary for eye-safe operation at close range. The NDF also separates off a portion of the output power, which is measured by power meters in order to monitor the laser output.

The transmitted beam is coaxially aligned with the receiver optics and is reflected

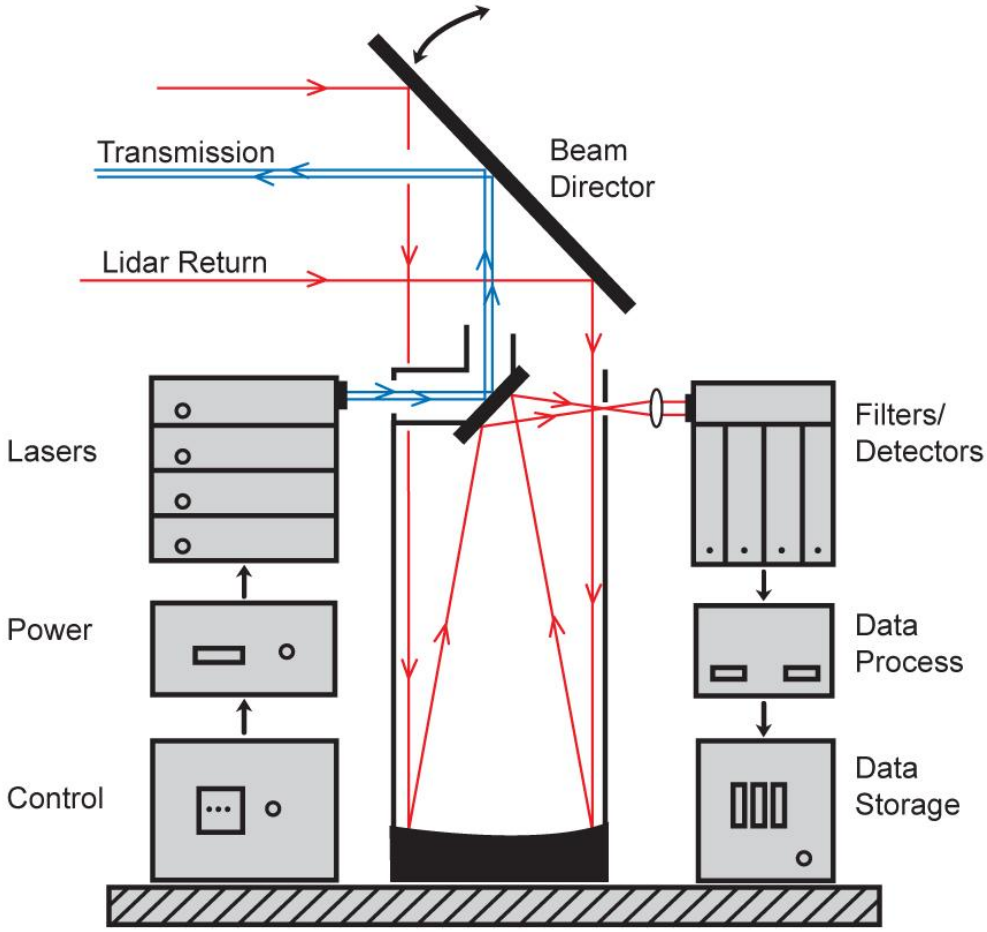

Fig. 1.1: Lidar conceptual drawing.

off of a turning mirror before leaving the lidar. The laser beam is scattered by the target, and signal is then received by the lidar. The received signal is reflected off of the turning mirror and into the receiver telescope.

The receiver telescope passes the signal on as a collimated beam. This beam passes through dichroic filters, which separate out different components of the signal. The different wavelengths pass through appropriate filters before passing on to the detectors. The ultra-violet and visible components are detected using photo-multiplier tubes (PMT), while the infra-red component is focused onto an avalanche photo-diode

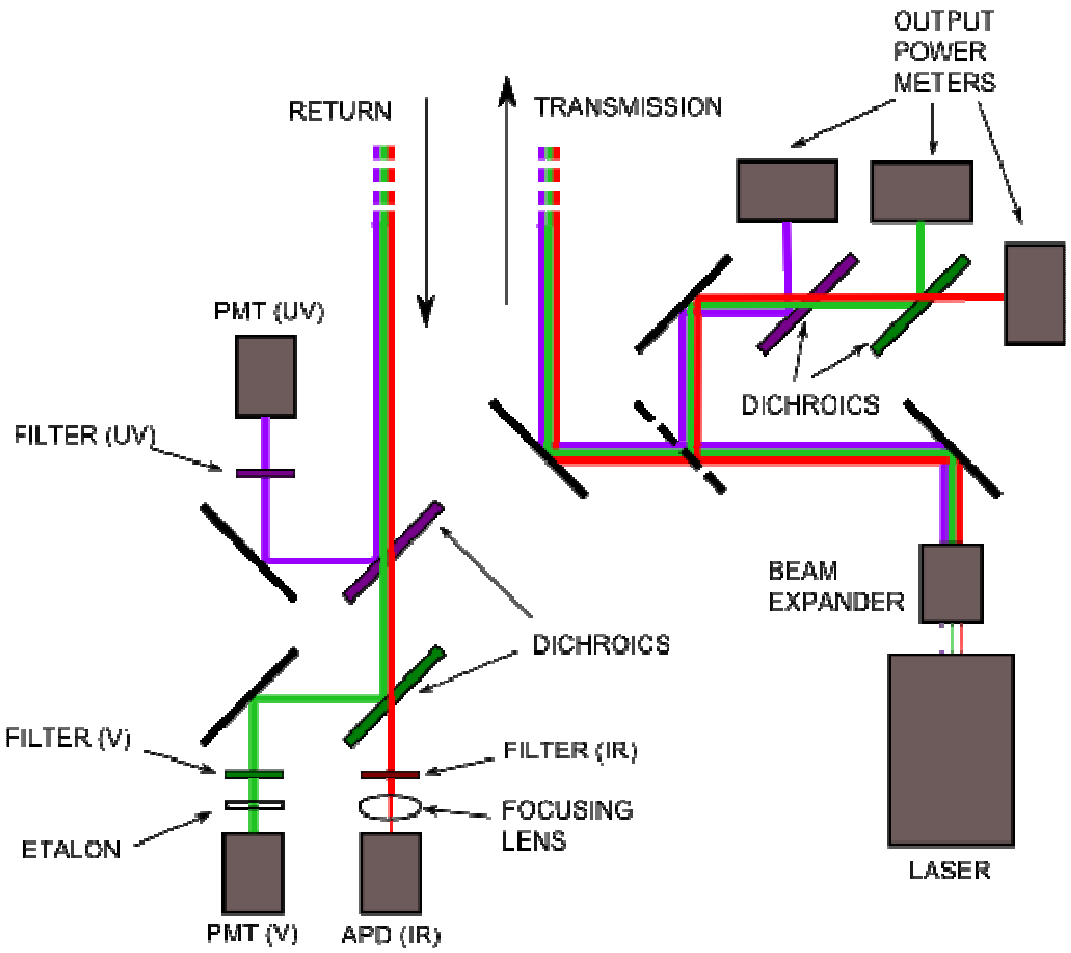

Fig. 1.2: Optical bench setup.

(APD).

The control unit contains the electronics and computer that control the lidar and collect and store the measurements made by the instrument. A user defines the parameters of an experiment at the control unit, including the scan pattern, scan duration, and measurement resolution. The control unit then automatically collects the data [7].

The air regulation system consists of a filtered blower unit and an air conditioner. The blower creates positive pressure within the optics unit. This helps keep out dust, which can contaminate the optical components, and also helps keep out insects, which

can damage the laser. The air conditioner keeps the internal temperature of the trailer within the range required for operation of the laser. In the case of cold temperatures, portable heaters are brought into the trailer.

In addition to the computer in the lidar control unit, two other computers are located in the lidar trailer. One computer displays video images of the lidar observation path for safety monitoring, and the other computer runs the lidar retrieval program, converting lidar data into pollutant values.

C. *Role of the Retrieval Program*

The purpose of the Aglite system is to provide accurate high temporal and spatial resolution measurements of the total emission of an agricultural site or operation. Both lidar scans and measurements using conventional instruments are taken. Every instrument measures a different specific aspect of the total emission. The role of the retrieval program is to combine the data from the various instruments, perform necessary signal processing, and calculate the total emission.

The lidar data retrieval program can be broadly described by three general steps. Both the lidar information and data from the other instruments are presented from the perspective of how they enable the retrieval of the aerosol conentrations. The first step is to calibrate the lidar using the conventional instruments. Secondly, the lidar retrieval algorithm is used to generate maps of particulate mass concentration in the atmosphere around the facility. Finally, the particulate mass concentration data are merged with meteorological data to calculate the emission rate as a function of time.

The Aglite instrument has not been absolutely calibrated from first principles. An

unknown amount of attenuation of the lidar signal takes place within the instrument. This attenuation depends on many complex factors, including the configuration and parameters of the receiving optics, and the efficiency of the optical detectors. Several of these factors, particularly the parameters of the receiver telescope, can also drift from campaign to campaign. Uncertainty in these factors means that it is most practical to calibrate the lidar returns against conventional instruments

During the campaign, the lidar is directed past a point where a particle sampler and OPC instrument are located. The point sensors give absolute aerosol concentration at that point, which in turn allows the lidar signal to be calibrated.

D. *Chapter Overview*

The rest of this thesis is organized into three chapters describing in detail the operation and results of the retrieval program used with the Aglite instrument. Additionally, references are listed at the end of the thesis.

Chapter 2 describes the operation of the retrieval program mentioned previously. Each step of the retrieval process is described. In addition to lidar data, processing of the in situ data is described, as well as its incorporation into the retrieval algorithm. The algorithm is described in detail, along with general description of its mathematics.

Chapter 3 presents the results of the measurements made by the instruments on the first field campaign. This campaign was made in Ames, Iowa, at a swine grower/finisher CAFO. The emissions from the facility are described.

Chapter 4 concludes with a discussion of the factors that impact the performance of the instrument. The weaknesses of the retrieval algorithm are described as are

logistical steps for mitigating these problems. Areas for future improvement of the algorithm are mentioned.

CHAPTER 2

AEROSOL CHARACTERIZATION

A. *Importance and Assumptions*

Data from in situ point sensors are essential to calibrate the mass concentration measurements of the lidar. The lidar equation [8], which describes the lidar signal as a function of range z for wavelength λ, is

$$P_\lambda(z) = P_0 \cdot L \cdot \frac{c\tau}{2} \cdot A_\lambda(z) \cdot \frac{\beta_\lambda(z)}{z^2} \cdot \exp\left(-2\int_0^z \sigma_\lambda(z')\partial z'\right). \qquad (2.1)$$

The term $P_\lambda(z)$ is the measured lidar power for distance z, and is measured in photon counts. P_0 is the output power of the lidar, L is the lidar coefficient representing system efficiency, c is the speed of light, τ is the pulse width of the lidar, $A_\lambda(z)$ is effective area function, also known as the geometric form factor (GFF), $\beta_\lambda(z)$ is the atmospheric optical parameter called the backscatter coefficient, and $\sigma_\lambda(z)$ is the atmospheric optical parameter called the extinction coefficient. The backscatter and extinction coefficients are functions of temperature, pressure, humidity, and the background and pollutant aerosols. Their effects are described in more detail in chapter 3.

As will be described in this chapter, the solution of (2.1) requires knowledge of the optical parameters of the background atmosphere and knowledge of the optical parameters of both the background and pollutant at some reference point. This information is provided by the in situ point sensors. Particle samplers and OPC point sensors are co-located with the lidar beam to establish the reference point, while additional point sensor instruments placed at other locations assist in providing the other

necessary information, including certain size distribution parameters of the aerosols.

An aerosol is characterized by a multitude of parameters. Prominent parameters include particulate concentration, the particle size distribution, complex index of refraction, and effective density. While the lidar is well suited for measuring relative particulate concentration, the other parameters must be constrained using in situ instruments and certain assumptions.

The main assumptions made in the lidar retrieval process are: the aerosol size distribution is bi-modal lognormal, aerosol particles are spherical, and the aerosol index of refraction, mode radii, and mode geometric standard deviations are constant in time and space. The mode radius describes the peak value of a mode, while geometric standard deviation describes the width of a mode. It is understood that these assumptions may not always hold, but they are necessary to enable the lidar data retrieval.

The standard units of measurement used by the EPA for aerosol concentration are called “Particulate Mass 2.5” ($PM_{2.5}$), “Particulate Mass 10” (PM_{10}), and “Total Suspended Particulate” (TSP). $PM_{2.5}$ is defined as the cumulative mass of all aerosol particles with an aerodynamic diameter less than 2.5 μm, PM_{10} is defined as the cumulative mass of all aerosol particles with an aerodynamic diameter less than 10 μm, and TSP is defined as the total mass of aerosol particles ranging from zero to infinity. For the in situ OPCs, TSP is limited to particles of around a millimeter or less in diameter by a protective screen on the intake of the instruments, and by the fact that larger particles have a very high settling velocity.

PM can be expressed as a function of the particle size distribution and particle mass. Here is shown the general expression of PM for spherical particles,

$$PM_D = \frac{\pi}{6}\rho\int_0^D d^3 n(d)\partial d \,. \qquad (2.2)$$

The term d is the diameter of a sphere and ρ is the density of the aerosol material. The term D is the aerodynamic cutoff diameter and may take values of 2.5e-6, 10e-6, or ∞. A relationship between physical radius and aerodynamic diameter has been described for particles of aerodynamic diameter greater than one micron [9], which is shown here,

$$D = \sqrt{\rho}\cdot d \,. \qquad (2.3)$$

B. *OPC Data*

The parameters of a lognormal distribution are the mode radius, also called the geometric mean radius, and the geometric standard deviation. These parameters are distinct for each mode of the distribution. The values of these parameters are required for the lidar retrieval, so it is necessary to extract values for them using data from the OPC instruments before the lidar data analysis can continue.

An OPC instrument draws in ambient air and counts the number of particles in the flow using an optical sensor. The instrument can discriminate particles by size. A single measurement report by an OPC consists of an array of particle counts per sample volume. The MetOne OPC instrument sorts the particles into eight size bins according to diameter, 0.3, 0.5, 0.6, 1.0, 2.0, 2.5, 5.0, and 10 microns. The sorted particle count value in each bin is the number of particles measured per sample volume that have a diameter greater than a certain threshold. The particle counts are summed and reported every 20 seconds at the current instrument settings.

The first step in the analysis of the OPC data is to normalize the particle counts to

particles per cubic meter. This is done by dividing the number count by the sample volume, as shown here,

$$\tilde{N} = \frac{N_{meas}}{V_{sample}}. \tag{2.4}$$

Standard pressure and temperature are defined by the instrument manufacturer. An example of normalized particle counts is shown in fig. 2.1(a).

At this point, each value in the particle count array represents the total number of particles greater than a certain diameter. This is the same as the integral of the particle size distribution from d' to infinity.

$$\tilde{N}(d') = \int_{d'}^{\infty} n_{opt}(d_{opt}) \partial d_{opt} \tag{2.4}$$

The standard way of dealing with this data is to process the data in discrete form and express them as a log-normalized size distribution. This is illustrated by fig. 2.1(b). The particle counts have been segregated into particle size ranges. The log normalized particle size distribution is typically expressed in the form below,

$$n_{\log}(d_{opt}) = \frac{\partial N(d_{opt})}{\partial \ln|d_{opt}|}. \tag{2.5}$$

In this form, it is assumed that the value of the log-normalized distribution is constant over each size range. This interpolates values for the distribution function along each size range and allows the distribution function to be defined for any value of d_{opt}. This makes the distribution function continuous with any size range. Dividing the log-normalized distribution by d_{opt} yields the particle size distribution. This is shown in fig. 2.1(c).

$$n_{opt}(d_{opt}) = \frac{n_{\log}(d_{opt})}{d_{opt}} \tag{2.6}$$

An alternative method of calculating the particle size distribution is to differentiate (2.4) with respect to diameter, which yields the following equality,

$$n_{opt}\left(d_{opt}\right) = -\frac{\partial \tilde{N}}{\partial d_{opt}}. \tag{2.7}$$

Due to the coarseness of the particle count data, it is necessary to interpolate between the measured values before the numerical derivative can be computed. This process yields the particle size distribution of aerosol as measured by the OPC. Figure 2.1(d) shows a comparison of the particle size distributions yielded by this method and by

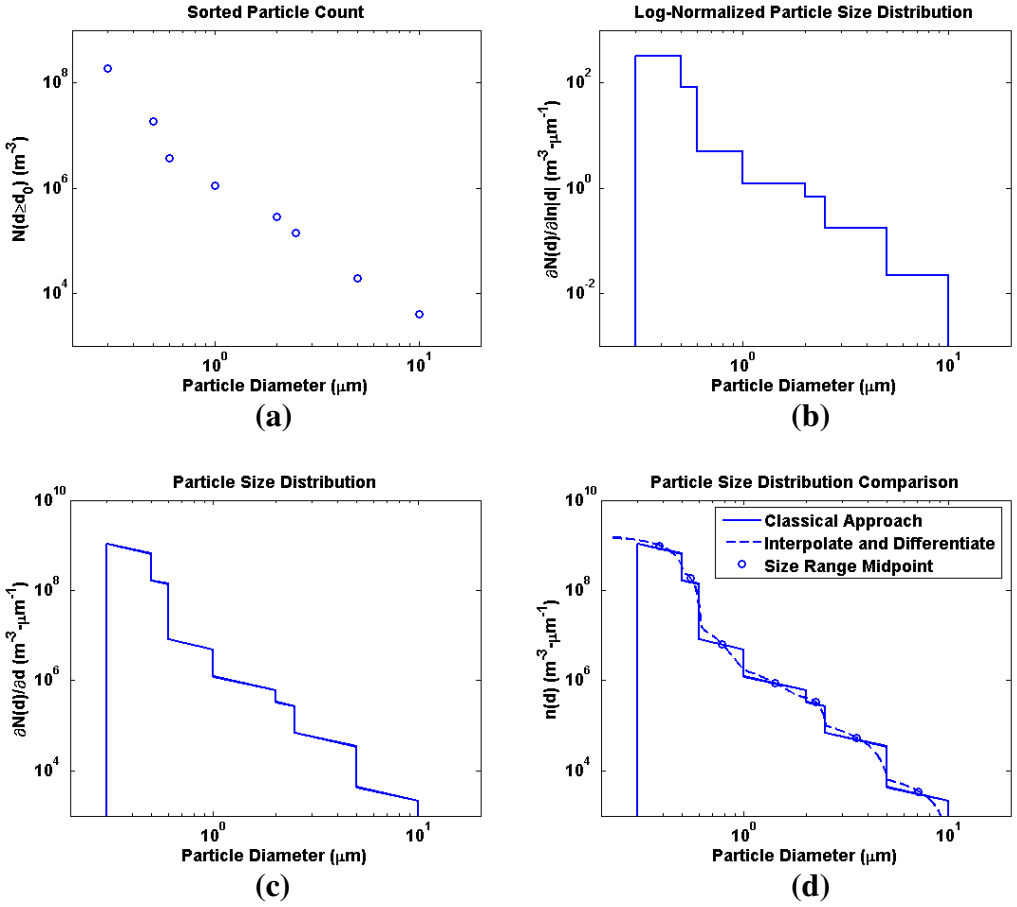

Fig. 2.1: OPC processing steps.

the standard method.

Since OPC instruments detect particles optically, the particle size distribution yielded from OPC data is in terms of effective optical diameter, or d_{opt}. For spherical particles, one expects d_{opt} to equal d, while for non-spherical particles d_{opt} is larger than d. If we define the relationship $d_{aero} = l \cdot d$, and if the particle size distribution derived from the OPC data is converted to particle volume distribution, this can be integrated to give total particle volume for a size range. Since PM is regulated based on aerodynamic radius, we define the relationship $d_{opt} = k \cdot d$, and we can define the total particulate volume in a certain PM range with the following,

$$Vol_D = \frac{\pi}{6 \cdot k^4} \int_0^{D \cdot k / l} d_{opt}^3 n_{opt}\left(d_{opt}\right) \partial d_{opt} \ . \qquad (2.8)$$

C. *Particle Sampler Data*

Particle samplers are co-located with the OPC instruments. A particle sampler instrument intakes air through a aerodynamic size-separating impactor head and pulls it through a filter, which has been previously weighed. The impactor head selectively allows particles below a certain effective aerodynamic radius pass through to the filter. Particles that pass the impactor are collected on the filter as gasses are pulled through it. The filter is then removed and weighed. The difference in filter weight, combined with the flow-rate of the instrument, gives a direct measurement of PM value in $\mu g/m^3$. If the aerosol particles are assumed to be spherical, an expression similar to (2.2) may be used to describe the measurements of a sampler instrument. Since the impactor head discriminates based on aerodynamic properties of the aerosol, the integration is not

performed on all particles up to a given actual diameter, but rather on all particles with an effective aerodynamic diameter $d_{aero} \le D$. We can modify (2.1) to the following form,

$$PM_D = \frac{\pi}{6}\rho \int_0^{D/l} d^3 n(d) \partial d \,. \tag{2.9}$$

The effective density of the aerosol material can be calculated by dividing the mass measured from a particle sampler by the volume measured from a co-located OPC instrument. Dividing the PM in a certain size range by the volume measured in that size range yields an effective aerosol particle density for the particles in that size range, shown here as

$$\rho_d = \frac{PM_d}{Vol_d} = \frac{k \cdot \rho \int_0^{l \cdot d} d^3 n(d) \partial d}{\int_0^{D \cdot k / l} d_{opt}^3 n_{opt}(d_{opt}) \partial d_{opt}} \,. \tag{2.10}$$

D. *Particle Size Distribution Parameters*

The particle size distributions of atmospheric aerosols are often described as a multi-mode lognormal distribution [10]. It is desirable to determine the parameters of a measured distribution for processing lidar data. In the context of lidar data in this thesis, particle size is given in terms of radius. A bimodal lognormal distribution is described as follows,

$$n(r) = \frac{N_1}{\sqrt{2\pi} r \ln|\sigma_1|} \exp\left[-\frac{1}{2} \frac{\ln|r/\mu_1|}{\ln|\sigma_1|} \right] + \frac{N_2}{\sqrt{2\pi} r \ln|\sigma_2|} \exp\left[-\frac{1}{2} \frac{\ln|r/\mu_2|}{\ln|\sigma_2|} \right]. \tag{2.11}$$

The terms N_1 and N_2 represent the number of particles in their respective modes. The terms σ_1 and σ_2 are the geometric standard deviations, and μ_1 and μ_2 are the mode

radii of their respective modes.

The parameters that best describe the aerosol are those parameters whose particle size distribution most closely matches the data from the in situ instruments. The process for determining those parameter values is outlined here.

Arbitrary initial parameter values are selected. From these values, a particle size distribution is constructed. From this, particle size distribution values and ratios of PM_{10} and PM_{TSP} to $PM_{2.5}$ are calculated. The actual measurements from the OPC and sampler instruments are compared against these calculated values and the error is calculated, using the following equation,

$$E = \left(\ln|n| - \ln|\hat{n}|\right)^T \cdot W \cdot \left(\ln|n| - \ln|\hat{n}|\right) + \alpha\left(m_{10} - \hat{m}_{10}\right)^2 + \beta\left(m_{TSP} - \hat{m}_{TSP}\right)^2$$

$$\alpha = \frac{\sum_{i=1}^{m} \ln|r_i|}{\rho_{10}} \qquad \beta = \frac{\sum_{i=1}^{m} \ln|r_i|}{\rho_{TSP}} \qquad W = \begin{vmatrix} r_1 & & & \\ & r_2 & & \\ & & \ddots & \\ & & & r_m \end{vmatrix}. \qquad (2.12)$$

The term *r* represents radius values for which there are OPC particle size distribution values, while the term *n* is a vector of particle size distribution values measured at the points described by *r*. The term m_{10} is the ratio of PM_{10} to $PM_{2.5}$, while the term m_{TSP} represents the ratio of PM_{TSP} to $PM_{2.5}$.

Each of the parameters of the particle size distribution is then varied by some small perturbation, and an error value is calculated for each perturbation. The perturbation that resulted in the lowest error is selected, and the corresponding parameter is set to its new value. This is repeated until convergence, at which point resulting particle size distribution parameters are selected as the parameters describing the aerosol.

An example of a particle size distribution that has been fit to in situ data is shown in fig. 2.2.

E. *Meteorological Data*

Two sets of meteorological instruments are used by Aglite, tower mounted weather stations and a separate suite of instruments attached to a tethered balloon. These include cup anemometers and weather vanes for measuring wind direction and speed, barometers, and temperature and humidity sensors. The balloon instruments are raised and lowered during the measurement time period in order to extend the vertical profiles of wind direction and speed, temperature, and humidity above what is measured by the

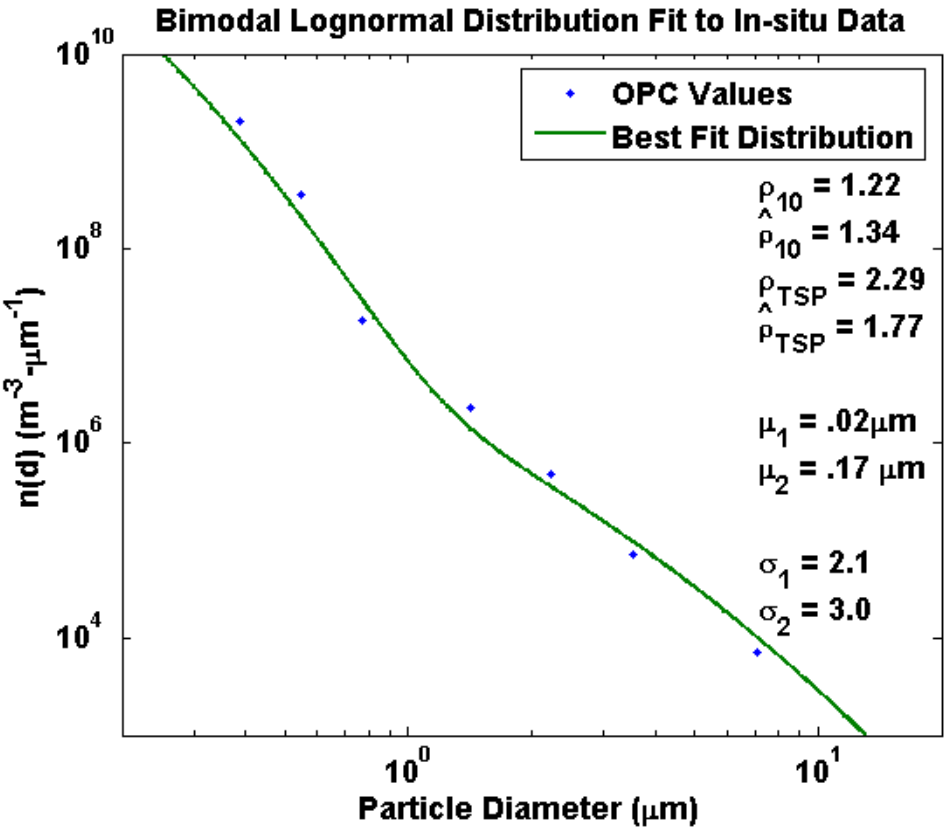

Fig. 2.2: Bimodal lognormal distribution fit to in situ data.

tower mounted weather stations. The balloon is typically raised to 500 ft (150 m) Depending on the location of a campaign, FAA regulations may limit the height of balloon operation to 500 ft.

Temperature, humidity, and pressure measurements are used in calculating the background optical parameters of the atmosphere. Wind direction and speed are used in combination with lidar measurements to calculate emission rates.

CHAPTER 3

RETRIEVAL PROGRAM DESIGN

The role of the retrieval program is to convert the data taken by the Aglite system into distributed aerosol concentrations. Raw lidar data consist of range-gated power measurements from photon detectors. Included with this data is information about time and pointing direction. The desired product of the retrieval program is aerosol mass concentration.

Aerosol calculations and meteorological data are collected using the auxiliary instruments described previously. This additional data characterizes the aerosol under investigation and the background atmosphere at discrete points.

The entire retrieval process is performed in the Matlab environment. Matlab was chosen for its ease of development. Currently, the retrieval process is not performed until after the completion of a field campaign. Retrieval speed is therefore not paramount. It is planned that in the future, near real-time retrievals will be required and the retrieval program will be ported to a compiled programming language, such as C++.

The first step of the retrieval program is to preprocess the data from both the conventional instruments and the lidar. The data are converted into Matlab format and filtered. Optical parameters of the pollutant and of the atmospheric background are determined using data from the conventional instruments. The physical parameters of the particle size distribution of the background and pollutant aerosols are calculated. Background Rayleigh scattering is calculated using the meteorological data. This coincident data developed by both sets of instruments are what allow the calibration of

the lidar data.

Secondly, the retrieval algorithm is used to convert the lidar data from photon counts to atmospheric optical parameter values, either backscatter or extinction, using the optical parameters previously determined. The data are then converted from optical parameter values to total particulate mass concentration using inverse Mie theory, with particle size distribution parameters that were measured by the in situ instruments. The lidar data are then resampled and interpolated to make them ready for integration with wind data.

Lastly, the lidar data are combined with wind speed data to calculate the particle flux. This particle flux is integrated and averaged over time. The difference between the downwind and the upwind total flux is the net emission of the agricultural operation.

A. *Lidar Data Preprocessing*

1) *Range Corrected Logarithmic Adjustment*: The lidar equation is described by (2.1), however the actual signal measured by the lidar also includes a noise term. This noise term for an individual pulse measurement can be modeled by a Poisson random variable. A lidar data measurement is made by integrating the signal from individual pulses from a specific angle over some integration time. Typical integration times are between 0.1 and 10 seconds. This means a single data measurement is the sum of between 1,000 and 100,000 individual pulse measurements. The noise term for an integrated data measurement is in turn modeled by the sum of *M* Poisson random variables. Following the Central Limit Theorem, this noise term is approximated as a Gaussian random variable with expected value $\overline{N}_{\lambda}$ and variance σ_N^2. The actual signal

for a channel λ is represented here,

$$\tilde{P}_\lambda(z) = \sum_{i=1}^{M} P_{\lambda i}(z) + \sum_{i=1}^{M} N_{\lambda i} \,. \tag{3.1}$$

The noise term introduces a DC component into the lidar data that must be taken into account. At large distances, z > 10 km, the signal $\tilde{P}_\lambda$ is dominated by noise. The DC component can be estimated using the expected value of the noise by calculating the mean value of the signal after 10 km,

$$E[N_\lambda] \approx \overline{N}_\lambda = mean\left(\tilde{P}_\lambda(z), z \geq 10km.\right). \tag{3.2}$$

The noise bias is removed from the data by subtracting the DC component from the integrated data measurement

A useful form of the lidar equation is the range-normalized power, here called the X-function. The X-function of the actual signal is found by first subtracting the expected value of the noise term and then multiplying the result by the range squared, as shown here,

$$X_\lambda(z) = z^2 \cdot \left(P_\lambda(z) + N_\lambda - E[N_\lambda]\right)$$

$$E[X_\lambda] = E\left[z^2 \cdot \left(P_\lambda(z) + N_\lambda - E[N_\lambda]\right)\right]$$

$$E[X_\lambda] = z^2 \cdot \left(P_\lambda(z) + E[N_\lambda] - E[N_\lambda]\right) = z^2 \cdot P_\lambda(z). \tag{3.3}$$

The variance of X_λ is given as follows:

$$\sigma_x^2 = E\left[X_\lambda^2\right] - E[X_\lambda]^2$$

$$\sigma_x^2 = E\left[z^4\left(P_\lambda^2 + 2P_\lambda\left(N_\lambda - \overline{N}_\lambda\right) + \left(N_\lambda - \overline{N}_\lambda\right)^2\right)\right] - z^4 \cdot P_\lambda^2$$

$$\sigma_x^2 = E\left[z^4 \cdot \left(N_\lambda - \overline{N}_\lambda\right)^2\right]$$

$$\sigma_x^2 = z^4 \cdot \sigma_N^2 . \tag{3.4}$$

A more convenient form is the logarithmic range-normalized power shown in (3.5). This is formed by subtracting the DC noise component from the original signal, range-correcting the signal, and taking the natural log of the result. These steps are illustrated in panes (a), (b), and (c) of fig. 3.1.

$$S(z) = \ln\left|X_\lambda\right|$$

$$S(z) \cong \ln\left|P_0 \cdot L \cdot \frac{c\tau}{2} \cdot A_\lambda(z)\right| + \ln\left|\beta_\lambda(z)\right| - 2\int_0^z \sigma_\lambda(z')\partial z' \tag{3.5}$$

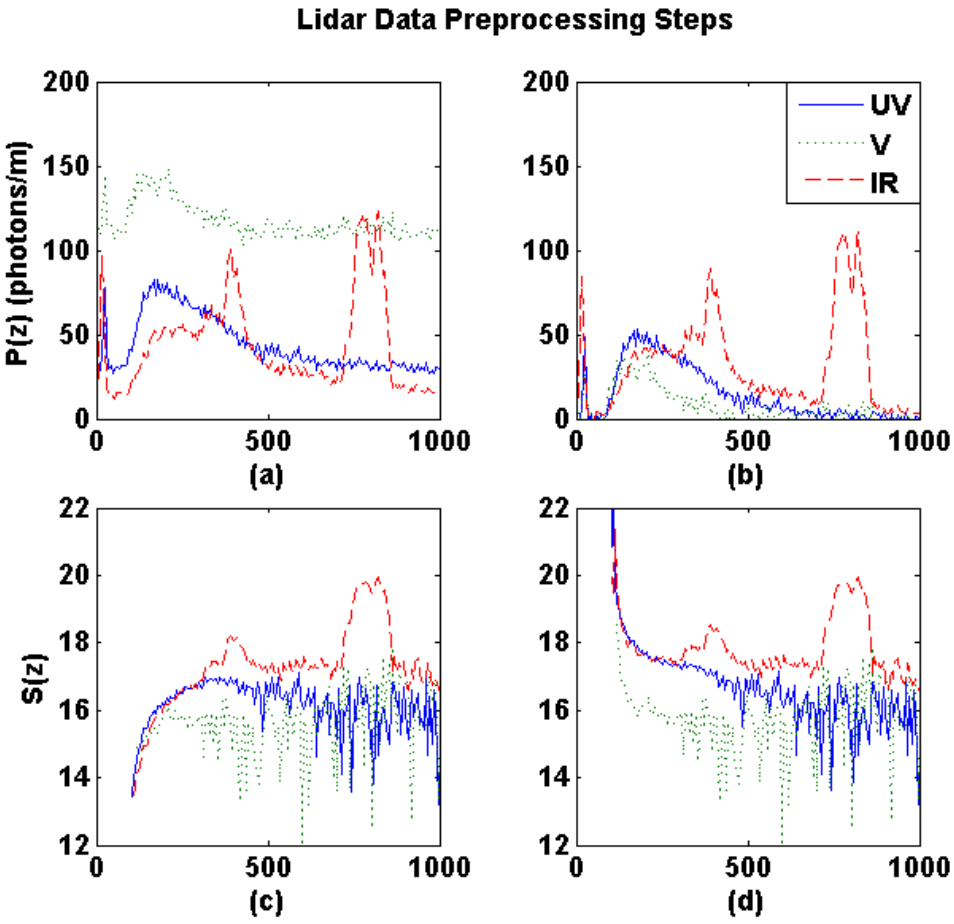

Fig. 3.1: Lidar data preprocessing steps.

2) *Geometric Form Factor*: In (2.1), the term A_λ represents the geometric form factor (GFF), which is dependent on z. This term represents the fraction of return signal that is viewable due to the geometry of the receiver optics. It is described by the following equations [10]:

$$A(z) = \frac{2\pi r_0^2}{W^2}\int_0^{r_T} \xi(z)\exp\left(-\frac{r^2+d^2}{W^2}\right) I_0\left\{\frac{2rd}{W^2}\right\} r dr$$

$$\xi(z) = \frac{\alpha(r_a, r_c, r_f) - \alpha(r_a, r_c', r_f')}{\pi r_c^2}$$

$$\alpha(x,y,z) = y^2\psi_\alpha + x^2\psi_\beta - xz\sin\psi_\beta \qquad (3.6)$$

$$\psi_\alpha = \cos^{-1}\left(\frac{z^2+y^2-x^2}{2yz}\right) \qquad \psi_\beta = \cos^{-1}\left(\frac{z^2+x^2-y^2}{2xz}\right)$$

$$r_b' = r_b f / z \qquad r_f = rf / z \qquad r_c = r_0 f / z$$

where r_0 is the radius of the receiver lens or mirror, r_T is the radius of the area at range z visible to the receiver, r_a is the radius of the aperture, r_b is the radius of the obstruction, W is the laser beam radius at range z, and d is distance between the axis of the laser and the axis of the receiver optics at range z. The term I_0 is a modified Bessel function of the first kind. The function $\xi(z)$ is the geometrical probability factor. This term represents the proportion of the laser beam that is visible to the system optics. The term W can vary for the different channels of the lidar, making the effective area function wavelength dependent.

Both historically and in our experience with this lidar, calculation of the geometric form factor from telescope parameters is not reliable. The calculated shape of the GFF differs greatly from the true shape. It is often necessary to measure the GFF

experimentally. A method for doing so is described here [8].

The GFF term $A_\lambda(z)$ can be represented as $A_0 G_\lambda(z)$, where A_0 is the area of the telescope and $G_\lambda(z)$ is a normalized geometric form. The logarithmic range-normalized form (3.5) can be expanded to

$$S(z) = \ln\left|G_\lambda(z)\right| + \ln\left|P_0 \cdot L \cdot \frac{c\tau}{2} \cdot A_0\right| + \ln\left|\beta_\lambda(z)\right| - 2\int_0^z \sigma_\lambda(z')\partial z' . \qquad (3.7)$$

As illustrated in fig. 3.2, the function $A_\lambda(z)$ rapidly approaches the limit A_0, so $G_\lambda(z)$ rapidly approaches 1. The geometric form factor is expected to approach 1 at large

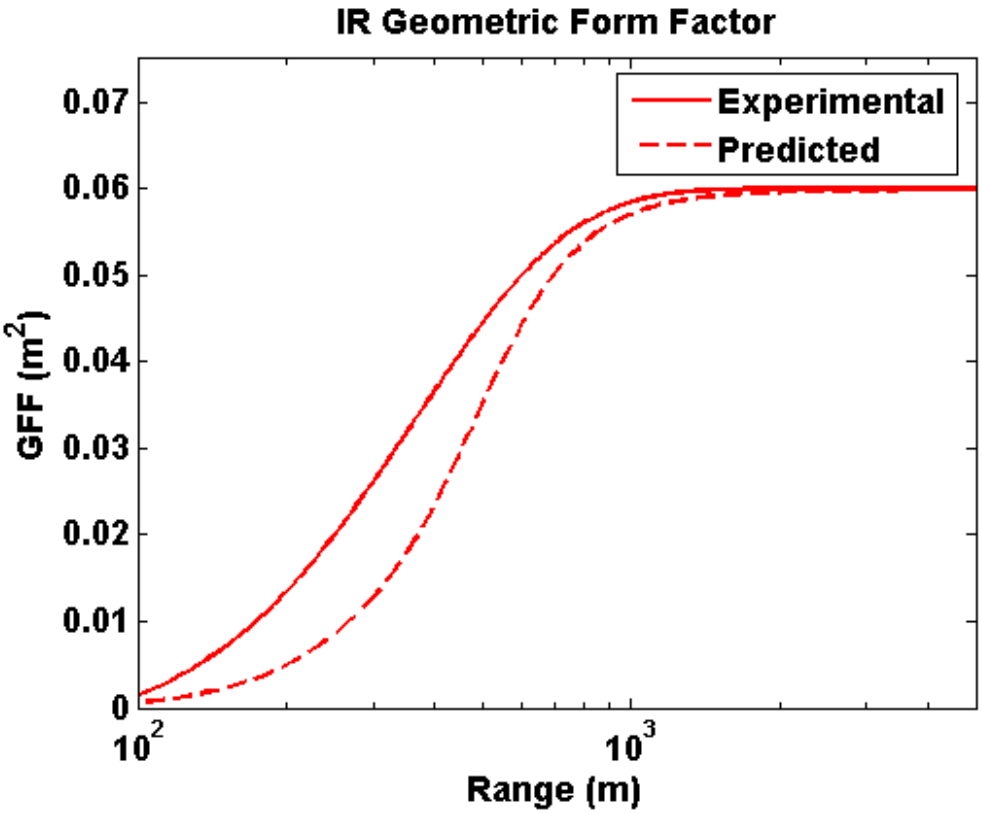

Fig. 3.2: Geometric form factor.

distances, so we may assume $\ln\left|G_\lambda(z)\right| = 0$ for values of z greater than some threshold z_0. The right-most terms of (3.7) can be written as a polynomial approximation.

$$S(z, z > z_0) \approx \ln\left|P_0 \cdot L \cdot \frac{c\tau}{2} \cdot A_0\right| + \ln\left|\beta_\lambda(z)\right| - 2\int_0^z \sigma_\lambda(z')\partial z'$$

$$S(z, z > z_0) \approx \sum_{n=0}^{N} C_n z^n \tag{3.8}$$

The normalized geometric form factor can now be approximated using the polynomial.

$$\log\left|\tilde{G}_\lambda(z)\right| = S(z) - \sum_{n=0}^{N} C_n z^n \tag{3.9}$$

Figure 3.2 shows the predicted GFF and the experimentally determined GFF for the IR channel of the Aglite lidar. The experimentally determined GFF has been smoothed to remove high frequency noise.

The effects of the term $A_\lambda(z)$ can be removed from the data by converting the data to the function described by (3.5), as shown in fig. 3.1(a,b,c), and then normalizing the data by subtracting (3.6), yielding the data in panel (d). This can be described as follows:

$$S(z) = \ln\left|P_0 \cdot L \cdot \frac{c\tau}{2} \cdot A_0\right| + \ln\left|\beta_\lambda(z)\right| - 2\int_0^z \sigma_\lambda(z')\partial z'. \tag{3.10}$$

3) *Digital Filtering*: Filtering is a necessary step in the retrieval process. Some noise reduction is provided by the integration time during the measurement itself (see (3.1)). After the data have been collected, a median filter and a 2D low-pass FIR filter are applied during preprocessing. Birds and insects can fly into the path of the lidar beam, creating large spikes in the raw data. These spikes can also be caused by stray branches

or obstacles impinging into the lidar beam when scanning near the ground. The median filter removes these spikes, which would otherwise be interpreted as large amounts of PM concentration.

The low-pass filter increases the stability of subsequent retrieval steps by removing high frequency noise from the signal. The aerosol size distribution retrieval step relies on the ratio of values of the channels, and the high noise levels in the UV and V channels make this step unstable. Filtering high frequency noise improves the stability of the retrieval. The data is visually inspected to determine minimum sizes of the aerosol structures and filter cutoff frequencies are determined accordingly.

B. *Backscatter Retrieval from Lidar Data*

1) *Lidar Differential Equation*: The lidar equation describes the power of the lidar return signal as a function of the range z. The two parameters in the lidar equation that characterize the optical characteristics of the atmosphere, extinction and backscatter, are denoted in the lidar equation by σ and β, both functions of range. We see that (3.5) may be written in the form of a partial differential equation [11].

$$\frac{\partial S}{\partial z} = \frac{1}{\beta(z)} \frac{\partial \beta(z)}{\partial z} - 2\sigma(z) \tag{3.11}$$

Over a region of homogeneous atmosphere, the term $\frac{\partial \beta}{\partial z}$ is equal to zero, and the homogeneous extinction term can be written as

$$\sigma(z) = -\frac{1}{2} \frac{\partial S}{\partial z}. \tag{3.12}$$

This is the basis of the so-called “slope method” lidar retrieval [12]. This method is only appropriate for homogeneous atmospheres.

Suppose the atmosphere consists of two components, a homogeneous background and a heterogeneous pollutant. Backscatter and extinction can be expressed as $\beta = \beta_a + \beta_b$ and $\sigma = \sigma_a + \sigma_b$. Let us further assume that the relationships between the backscatter and extinction components satisfy $\beta_a = B_a \cdot \sigma_a$ and $\beta_b = B_b \cdot \sigma_b$. The coefficient *B* is known as the "lidar ratio" of a scatterer, and (3.11) may be rewritten as

$$\frac{\partial S}{\partial z} = \frac{1}{(\beta_a + \beta_b)} \frac{\partial(\beta_a + \beta_b)}{\partial z} - 2\left(B_a^{-1}\beta_a + B_b^{-1}\beta_b\right). \tag{3.13}$$

The subscript *a* denotes the pollutant, and *b* denotes the background. Suppose a variable *S´* is defined as

$$S' = S + \frac{2}{B_b}\int_{z_0}^{z} \beta_b \partial z' - 2\int_{z_0}^{z} \frac{\beta_b}{B_a}\partial z' . \tag{3.14}$$

We see that (3.13) can now be rewritten in a form identical to (3.11)

$$\frac{\partial S'}{\partial z} = \frac{1}{\beta}\frac{\partial \beta}{\partial z} - 2\frac{\beta}{B_a} . \tag{3.15}$$

2) *Lidar Equation Solution*: The following is a solution of the differential equation described by (3.15). It was proposed by Klett as a solution to the lidar equation for two scattering atmospheric components [11],

$$\beta(z) = \frac{\exp(S')}{\frac{1}{\beta(z_0)} + 2\int_{z}^{z_0} \frac{\exp(S'(z'))\partial z'}{B_a(z')}} . \tag{3.16}$$

The denominator of Klett's solution contains a pole, which makes this solution unstable for range values greater than z_0. An alternative form of this solution to the lidar equation has also been demonstrated by Fernald [13], which has been shown to be equivalent to (3.16).

It is apparent that (3.16) requires *a priori* knowledge of the lidar ratios of both scatterers. It also requires knowledge of the backscatter value at some reference point. This knowledge is provided by the point sensors. Additionally, the point sensors provide information about the reference point, which acts to calibrate the lidar data at all other points.

3) *Pollutant Backscatter Estimation*: It is possible to estimate the backscatter values of the pollutant from the lidar data without using point sensors. This is useful for performing measurements in situations where it is infeasible to directly measure the target pollutant source using point sensor instruments.

Consider two points at $z = \alpha$, and $z = D$ on the same measurement, where the point D is completely free of pollutant aerosol. The relationship between these two points is given as follows.

$$S^a - S^D = \ln\left|\frac{\beta_a}{\beta_D}\right| + 2\int_a^D \sigma \partial z$$

$$\beta_a = \beta_D \exp\left(S^a - S^D\right)\exp\left(-2\int_a^D \sigma \partial z'\right) \tag{3.17}$$

This is illustrated in fig. 3.3. If the extinction is approximated by the background extinction, the pollutant backscatter can be computed directly. If the background aerosol on both sides of the pollutant plume is flat, lines can be drawn on both sides of the plume approximating the background signal. The offset between the two lines represents the integral of the extinction contribution from the pollutant plume. Using this estimate, the pollutant backscatter can be more accurately estimated.

4) *Rayleigh Scattering*: Elastic scattering in the atmosphere is divided into two

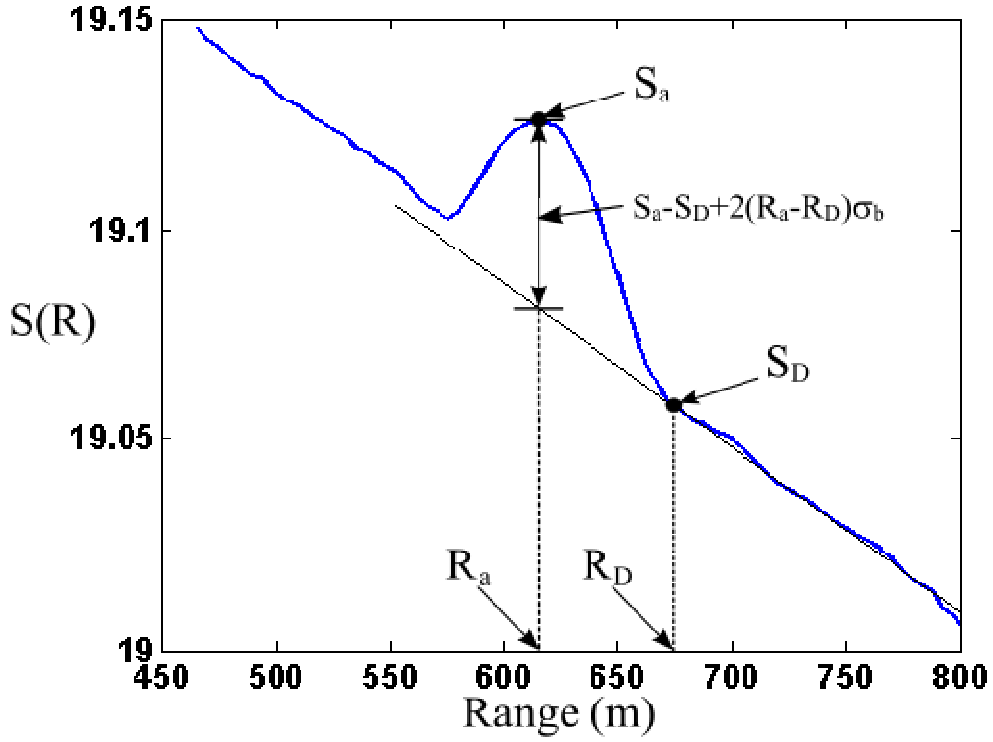

Fig. 3.3: Pollutant backscatter estimation.

regimes of interest, Rayleigh scattering and Mie scattering [14]. Rayleigh theory describes scattering by particles of dimension significantly smaller than λ, the wavelength of light, while Mie theory is used to describe scattering by particles of dimension on the order of λ.

Scattering by air molecules falls under the regime of Rayleigh scattering. The optical parameters described by Rayleigh scattering are functions of the density of air, the index of refraction of air, and the value of λ. Aerosols significantly smaller than λ do not contribute significantly to Rayleigh scattering. The expression for extinction is given by

$$\sigma = \frac{12\pi^3}{N'\lambda^4}\left(\frac{m^2-1}{m^2+1}\right)^2 \frac{6+3\Delta}{6-7\Delta}. \qquad (3.18)$$

The term N' is the concentration of molecules per unit volume, λ is the wavelength, m is the refractive index of air, and Δ is the depolarization factor for air. The lidar ratio of extinction over backscatter for Rayleigh scattering is always $8\pi/3$. It is clear from the λ term in (3.18) that the significance of Rayleigh scattering drops off rapidly as lambda increases. For example, Rayleigh scattering at the UV channel of the lidar (λ = 0.355 μm) is more than 80 times stronger than at the IR channel (λ = 1.064 μm).

5) *Mie Scattering*: The optical properties of aerosols are described by Mie scattering theory. The equations for extinction and backscattering by small spheres are given by

$$\beta(z) = \frac{1}{4}\int_0^\infty r^2 Q_\pi(r,\lambda,m)n(r,z)\partial r \qquad (3.19)$$

$$\sigma(z) = \int_0^\infty \pi r^2 Q_{ext}(r,\lambda,m)n(r,z)\partial r \,.$$

The functions Q_{ext} and Q_π are the extinction and backscatter efficiency functions. The function $n(r,z)$ is the particle size distribution function of the aerosol. As shown in (3.19), extinction and backscatter of an aerosol for a given wavelength are functions of particle size distribution and index of refraction of the aerosol. Particle size distribution and index of refraction are the aerosol characteristics for which the Mie equations must be solved. This is called the ill-posed inversion problem [15]. The resolution of the solution is limited by the number and wavelength values of the channels used by the lidar.

Examples of the extinction and backscatter efficiency functions are given for water-soluble particles in fig. 3.4. The indices of refraction for water-soluble particles were selected using values from the Air-Force Handbook [16]. The extinction and

backscatter efficiency functions calculated by Mie theory for the case of homogeneous spheres are given as

$$Q_{ext} = \frac{2}{k^2 r^2}\sum_{n=1}^{\infty}(2n+1)\mathrm{Re}(a_n + b_n) \tag{3.20}$$

$$Q_{\pi} = \frac{1}{k^2 r^2}\left|\sum_{n=1}^{\infty}(2n+1)(-1)^n (a_n - b_n)\right|^2$$

$$a_n = \frac{m\psi_n(mx)\psi_n'(x) - \psi_n(x)\psi_n'(mx)}{m\psi_n(mx)\xi_n'(x) - \xi_n'(x)(x)\psi_n'(mx)} \qquad b_n = \frac{\psi_n(mx)\psi_n'(x) - m\psi_n(x)\psi_n'(mx)}{\psi_n(mx)\xi_n'(x) - m\xi_n'(x)(x)\psi_n'(mx)}$$

$$\psi_n(\rho) = \sqrt{\frac{\pi\rho}{2}}J_{n+1/2}(\rho) \qquad \xi_n(\rho) = \sqrt{\frac{\pi\rho}{2}}H^{(2)}_{n+1/2}(\rho).$$

The function $J_{n+1/2}$ is the Bessel function of the first kind, order *n+1/2*. The function $H^{(2)}_{n+1/2}$ is the Hankel function with order n+1/2 and is defined as $H^{(2)}_{n+1/2} = J_{n+1/2} - iY_{n+1/2}$, where $Y_{n+1/2}$ is the Bessel function of the second kind.

The scattering by the background atmosphere has components from both Rayleigh and Mie scattering. Data from in situ instruments are fed into the equations describing Rayleigh and Mie scattering given above. The scattering of the background atmosphere is

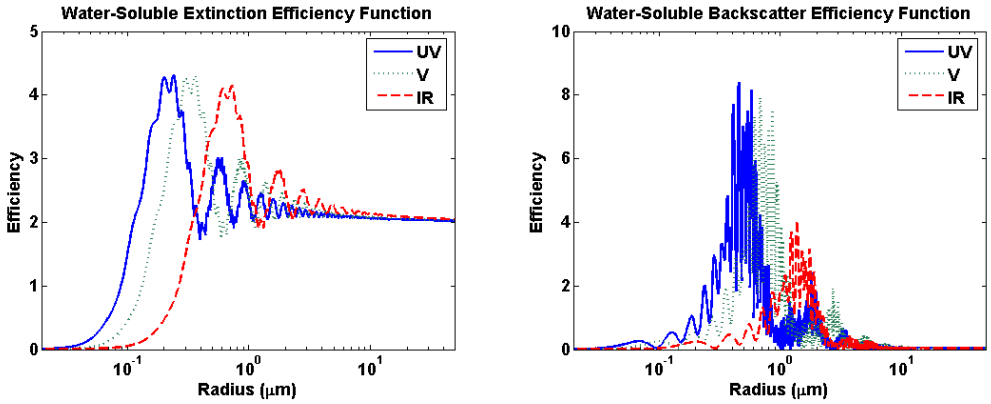

Fig. 3.4: Efficiency functions.

the sum of the Mie scattering and Rayleigh scattering effects. The lidar ratio of the background is thus given as the ratio of the sums of the backscatter terms over the extinction terms. The aerosol pollutant has only Mie scattering effects due to the relatively large size of aerosol particles.

$$\beta_b = \beta_{Rayleigh} + \beta_{Mie} \tag{3.21}$$

$$B_b = \frac{\beta_{Rayleigh} + \beta_{Mie}}{\sigma_{Rayleigh} + \sigma_{Mie}}$$

$$B_a = \frac{\beta_{Mie}}{\sigma_{Mie}}$$

Given the values of the parameters for background backscatter and background and pollutant lidar ratios, total backscatter can now be retrieved. These parameters are inserted into (3.19), which yields the total measured backscatter.

The stages of the lidar data retrieval are demonstrated in fig. 3.5; panel (a) shows the pre-processed lidar signal as a logarithmic range-normalized signal corrected for GFF, as described by (3.10), while panel (b) shows the same signal converted to backscatter using (3.16), and (d) shows the signal converted to PM values. The estimated value of the mode radius parameter is shown in (c).

C. *Aerosol Size Distribution Retrieval*

1) *Tikhonov Regularization*: The standard technique for solving (3.19) and retrieving particle size distribution is Tikhonov regularization. This technique is widely used with multi-wavelength lidars, however it has been disregarded for the Aglite instrument for two reasons. It has been shown to require at least four independent channels for acceptable retrievals [17], while the Aglite lidar has only three. Further, the

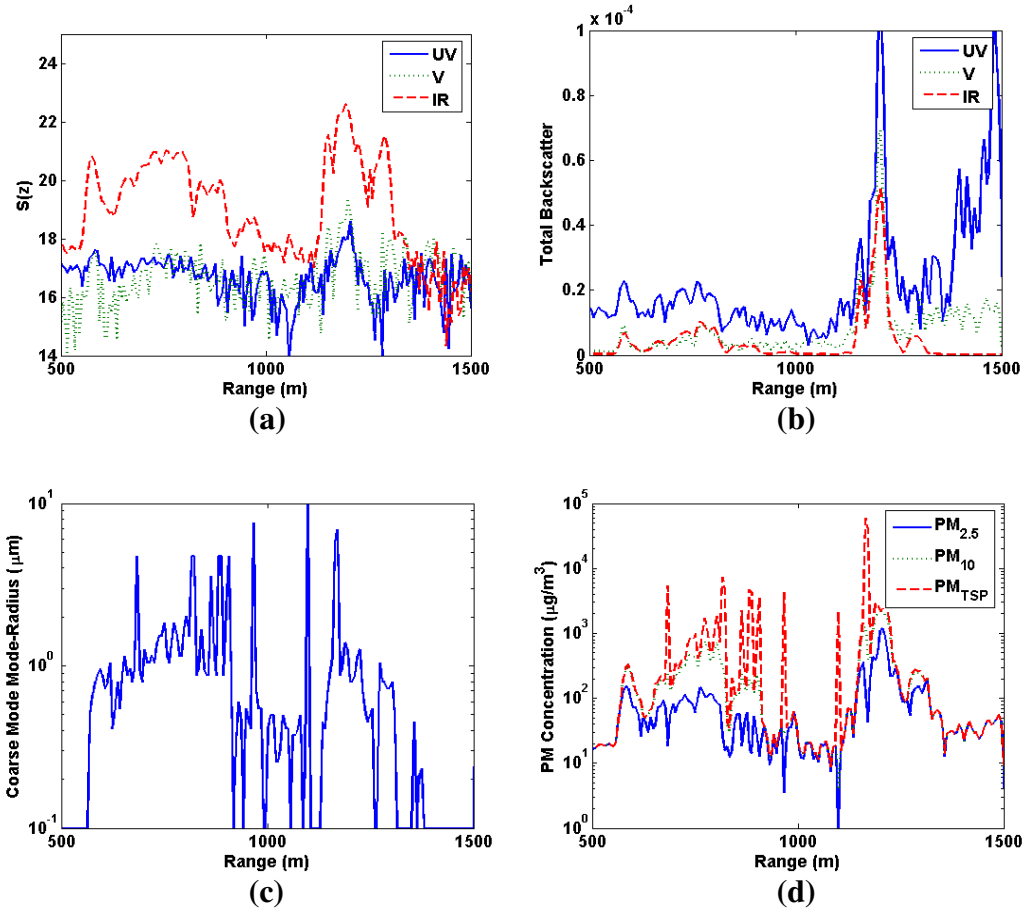

Fig. 3.5: Lidar processing steps.

constraints from the Aglite in situ instruments are difficult to incorporate into the Tikhonov method. In the future the Aglite lidar may be augmented with additional channels, allowing the use of Tikhonov regularization in retrievals. For this reason the method is briefly described here.

Several inversion techniques exist for solving the ill-posed inversion problem. Tikhonov regularization and graphical constrained parameter estimation are discussed here [17,18]. Both of these methods find, given certain constraints, the solution that minimizes the difference between measured data and the value of estimated data given by

the model.

The Tikhonov regularization method consists of reducing the expressions for extinction and backscatter shown by (3.19) to a set of first-order linear equations, and finding a minimum least-squares solution for the distribution function *n(r)*. The Mie equations can be written in the following form,

$$g_i = \sum_{j=1}^{n} w_{ij} K_{ij} f_j \ . \tag{3.22}$$

The term g_i is a backscatter or extinction parameter for a specific wavelength, w_{ij} is an integration weighting coefficient, K_{ij} is the coefficient corresponding to the efficiency function, and f_j is the coefficient corresponding to the particle size distribution function. The equations can now be written in vector form.

$$\mathbf{g} - \mathbf{e} = A\mathbf{f} \tag{3.23}$$

The term **g** represents the measured optical parameter vector, the *i*th term of which is the experimentally determined g_i, as defined above. The term $\hat{\mathbf{g}}$ represents the estimated value of **g**. The experimental uncertainty can be expressed as the difference between the measured and true values of the optical parameter vector.

$$\mathbf{e} = \hat{\mathbf{g}} - \mathbf{g} \tag{3.24}$$

Let it be assumed that there is some upper-bound on the magnitude of this error vector, where the magnitude is defined as a weighted inner product of some **f** with a symmetric matrix W.

$$\max\left|\mathbf{e}\right|^2 = E^2 = \left(A\mathbf{f} - \mathbf{g}\right)^T W \left(A\mathbf{f} - \mathbf{g}\right) \tag{3.25}$$

Let it further be assumed that we wish to impose a second constraint on our solution. This can be done by selecting an appropriate function $Q(\mathbf{f})$ and minimizing that function. The

constraint that is typically used is to minimize the norm of the second differences.

$$Q(\mathbf{f}) = \sum_{2}^{n-1} \left(f_{i-1} - 2f_i + f_{i+1} \right)^2 \tag{3.26}$$

This is expressible in matrix form as

$$Q(\mathbf{f}) = \mathbf{f}^T H \mathbf{f} \quad H = \begin{bmatrix} 1 & -2 & 1 & 0 & & & \\ -2 & 5 & -4 & 1 & 0 & & \\ 1 & -4 & 6 & -4 & 1 & 0 & \\ 0 & 1 & -4 & 6 & -4 & 1 & 0 \\ & & & & \ddots & & \\ & & 0 & 1 & -4 & 5 & -2 \\ & & & 0 & 1 & -2 & 1 \end{bmatrix}. \tag{3.27}$$

The problem is now expressible in a form solvable by a minimum least-squares solution.

$$J = \mathbf{f}^T H \mathbf{f} + \lambda \left(\mathbf{f}^T A^T W A \mathbf{f} - 2\mathbf{g}^T W A \mathbf{f} + \mathbf{g}^T W \mathbf{g} - E^2 \right) \tag{3.28}$$

Taking the gradient with respect to **f** and setting it equal to zero and letting $\gamma = 1/\lambda$, the solution to this equation can be written as

$$\mathbf{f} = \left(A^T W A + \gamma H \right)^{-1} A^T W \mathbf{g} \,. \tag{3.29}$$

The term γH embodies the constraints placed on the solution. Without this term, the solution would be made unstable by small Eigenvalues in $A^T W A$. The matrix H is full rank, and the size of the coefficient γ controls the stability of the solution. A value of γ that is too small will result in an unstable solution, while a value that is too high will over-constrain the solution. Therefore it is important to select the correct value for γ.

An estimate of the minimum value of γ can be obtained numerically. In order for the rows of (3.28) to be sufficiently linearly independent to produce a stable solution, the smallest Eigenvalue of $A^T W A$ must be at least twice as large as the ratio of the square norms of the vectors **e** and **f**. The constraint γ should be set larger than this value.

$$\gamma \geq 2\frac{\left|\mathbf{e}\right|^2}{\left|\mathbf{f}\right|^2} \tag{3.30}$$

2) *Graphical Constrained Parameter Estimation*: The second inversion technique described here is the graphical minimum least-squares method. It is the technique chosen for analyzing aerosol data from the Aglite system. This method consists of assuming a type of size distribution function for the aerosol, selecting suitable parameter ranges for the aerosol and its distribution function, and numerically finding the set of aerosol parameters that minimize the difference between the estimated and measured optical parameters [19].

Suppose the particle size distribution can be approximated as a combination of several size distribution functions. The estimated optical parameter vector can be broken up into a set of particle-normalized optical parameter vectors, corresponding to the separate distributions. Each particle-normalized optical parameter vector is multiplied by a coefficient that corresponds to the number of particles in that distribution. The estimate of **g** can thus be rewritten as follows:

$$\hat{\mathbf{g}} = \left|\tilde{\mathbf{g}}_1 \quad \tilde{\mathbf{g}}_2 \quad \cdots \quad \tilde{\mathbf{g}}_m\right| \begin{vmatrix} N_1 \\ N_2 \\ \vdots \\ N_m \end{vmatrix} = G\mathbf{n}\,. \tag{3.31}$$

Let a weighted inner-product with an induced norm be defined for the space of optical parameter vectors.

$$\left\langle \mathbf{a},\mathbf{b} \right\rangle = \mathbf{a}^T W \mathbf{b} \qquad \left|\mathbf{a}\right|^2 = \mathbf{a}^T W \mathbf{a} \qquad W = W^T \tag{3.32}$$

The value of the particle number coefficients that minimize the squared error

between the measured and estimated values of the optical parameter vector can be determined analytically by taking the gradient of the error with respect to **n** and setting it equal to the zero vector.

$$\frac{\partial}{\partial \mathbf{n}}\left|\mathbf{g}-\hat{\mathbf{g}}\right|^2 = 0 = -G^T W\mathbf{g} + G^T WG\mathbf{n} \tag{3.33}$$

$$\mathbf{n} = \left(G^T WG\right)^{-1} G^T W\mathbf{g}$$

We recognize this solution as the standard solution of a weighted minimum least-squares problem. This solution allows us to analytically determine the particle-number counts of a set of distributions, given all the remaining aerosol parameters.

Each particle normalized optical parameter vector $\tilde{\mathbf{g}}_i$ is a function of the distribution parameters of one of the component distributions of the aerosol. The matrix *G* is therefore also a function of the parameters of each of the components of the aerosol. Let the set of aerosol parameters be denoted by **S**. The estimate of the particle-number vector can thus be written as

$$\hat{\mathbf{n}} = \left(G(\mathbf{S})^T WG(\mathbf{S})\right)^{-1} G(\mathbf{S})^T W\mathbf{g}\,. \tag{3.34}$$

The set $\hat{\mathbf{S}}$ that most closely estimates actual values of the aerosol parameters can be determined by varying **S** until a minimum is achieved. External constraints can be imposed on the solution by fixing either the values of some of the elements of **S**.

$$\hat{\mathbf{S}} = \arg\min_{\mathbf{S}}\left|\mathbf{g} - G(\mathbf{S})\hat{\mathbf{n}}(\mathbf{S})\right|^2 \tag{3.35}$$

This technique is essentially the same as the technique described for extracting particle size distribution parameters from the in situ data. Any of the parameters previously extracted from the in situ data can be used as constraints on **S**.

The perturbation of **S** in search of the minimum can be performed two ways. One way is that the gradient of **S** can be calculated, yielding the direction of most decreasing error. The set **S** can then be perturbed this direction. Alternatively, each individual element of **S** can be perturbed in turn and the error values generated by each individual perturbation compared. The perturbation generating the lowest error is selected, and **S** is updated with this perturbation. For either method, the perturbation process is repeated until a minimum is achieved.

Aerosol particle size distribution in Aglite data is assumed to have a bimodal log-normal distribution, as described by (2.11). Because of the resultant complexity in calculating the gradient of (3.34), the second perturbation method described in the preceding paragraph was chosen for Aglite retrievals.

Once the parameters of the particle size distribution of an aerosol are known, it is trivial to calculate the particulate concentration. The particle size distribution is inserted into (2.2), and the PM values can be calculated. For Aglite lidar data, the particle size distribution, and therefore the PM values, can be calculated for every point in a lidar measurement.

D. *Algorithm Implementation*

The Aglite retrieval algorithm is currently implemented as a series of Matlab scripts, through which the data are successively passed. The retrieval steps are illustrated in fig. 3.6. Matlab was selected as the development environment due to the ease and quickness of development that it enables. As the Aglite system is used more frequently, there will be a need for a stand-alone program capable of processing the data in near-real

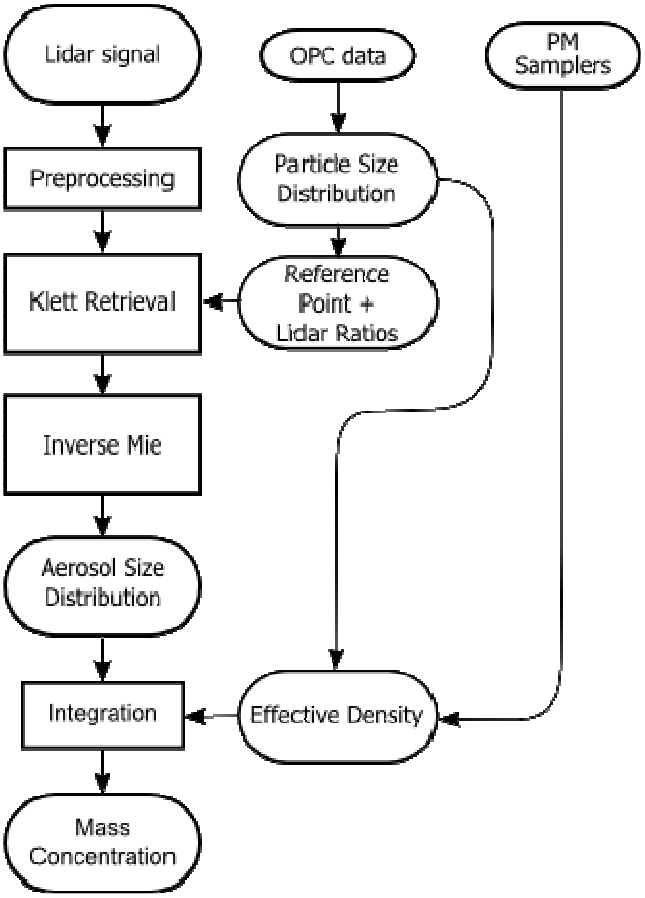

Fig. 3.6: Retrieval algorithm flow-chart.

time. It is anticipated that this need will be met in the future by an implementation of the algorithm in C++.

The initial data from the Aglite's Control Unit and OPC instruments are in the form of binary data files. These files are converted to Matlab format by means of a simple parser. A spreadsheet is created listing the start and end time of each set of lidar measurements. The OPC data are then processed as described in the previous subsection.

The OPC data are passed into a script, along with the start and end times of each set of lidar measurements and values from the PM samplers for the corresponding times. This script returns the particle size distribution parameters as measured by each OPC

instrument during the time frames of the lidar measurement sets. The script also gives the backscatter coefficients and lidar ratios for each OPC instrument and time frame. All of these values are stored in the spreadsheet. The meteorological information for each lidar measurement set is also stored in the spreadsheet.

Next, the lidar geometric form factor is calculated. A lidar measurement that was specifically taken for the purpose of calculating the GFF is fed into a script which estimates the GFF and stores it in a file.

The preprocessing, backscatter retrieval, and PM concentration retrieval are all performed in a single script. The lidar data in Matlab format and the retrieval parameters are fed into this script. The retrieval parameters include the GFF, the background aerosol backscatter and lidar ratio, the pollutant lidar ratio, and the pollutant particle size distribution parameters. After the preprocessing step, the data are visually inspected to select a suitable reference point. The script then finishes and outputs the PM concentration measurements.

CHAPTER 4

FIELD MEASUREMENTS

A. *Overview*

Here we present the initial results of the particulate emission characterization obtained by the Aglite lidar on its maiden campaign. The experimental work described was conducted at a deep-pit swine production facility situated near Ames, Iowa during a three week period in August and September of 2005. The goal of the campaign was to characterize the emission rate of the facility. The EPA measures and regulates pollution from concentrated animal feeding operations (CAFO) based on emission rates per animal unit. The currently accepted method for measuring emission rates is to build a software model of the facility, make a few point measurements using in situ instruments, and feed those measurements into the model. The lidar approach is to directly measure and integrate the total emission of the facility.

1) *Facility Description*: A schematic diagram of the deep-pit swine production facility and instrumentation employed on this site is shown in fig. 4.1. The facility consisted of three separate parallel barns, each barn housing around 1250 pigs with an average weight of approximately 90 lbs (40 kg) per animal. The area around the facility was topographically flat and surrounded by soybean and cornfields. An extended series of lidar and in situ observations were conducted during three weeks of data collection at this facility. Measurements were made day and night to capture the dynamics of particulate flux emissions. The local climate was typically characterized by clear skies, and winds were generally mild at 0-5 m/s, changing direction from west to south during

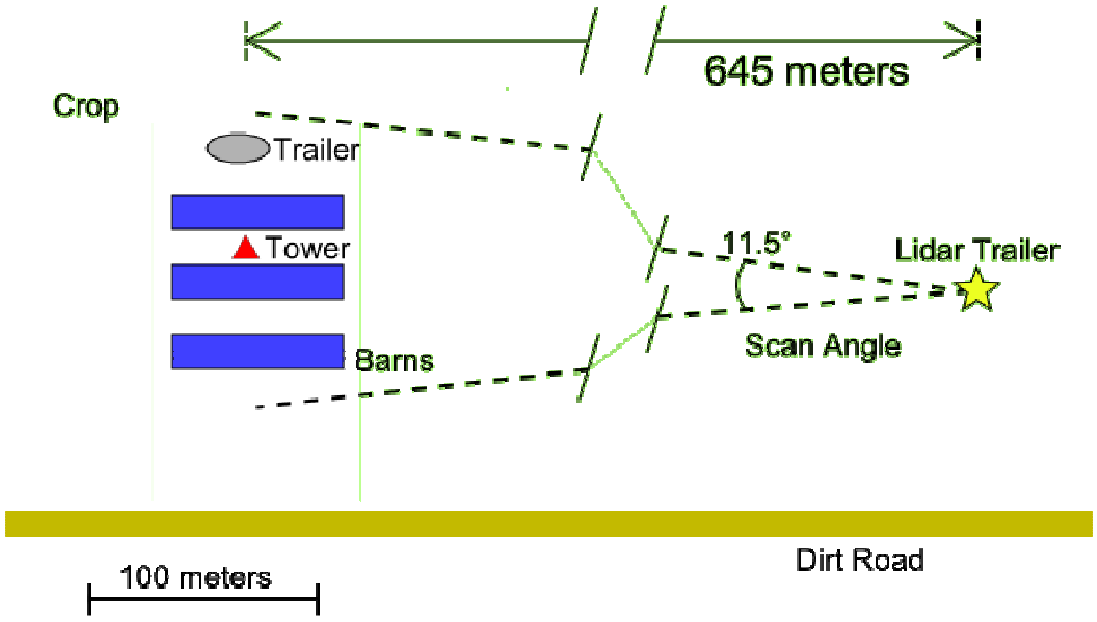

Fig. 4.1: Facility layout.

the study period. Lidar scan patterns included vertical scans between barns and on both sides of the barns and sensor trailer, horizontal scans above the barns at various elevations, and stationary stares measuring particulate emission in close proximity to the in situ instrumentation. These patterns of vertical and horizontal scans allowed the capture and monitoring of 3D distribution and temporal variations. Depending on the prevailing wind conditions, the measured particulate profiles varied significantly from day to day and occasionally even hour to hour. Two unpaved roads bordered the swine production facility, one running east to west about 115 m south of the central tower. The second road ran north to south at a distance of ~900 m west of the tower. Fugitive dust events from these roads occurred when vehicles drove past. These were captured during lidar observations and were included in the calibration procedure.

A number of OPCs were distributed around this swine facility. In addition, three were located on a central tower at heights of 3.6, 8.5, and 14.6 m, one was also located at

height of 4.1 m on a trailer located 60 meters downwind of the facility. A pair of Tisch Cascade impactors at the central tower and sensor trailer provided filter-based particle size fractionation and concentration measurements in the range of 0.37-9 μm. To measure chemical composition, real-time particle ionic composition, and fine particle size distribution, an Aerodyne Aerosol Mass spectrometer (AMS) was deployed at the trailer. Portable PM_{10} and $PM_{2.5}$ (AirMetrics MiniVol) samplers were co-located with the OPCs, and data from the samplers were collected on a daily-averaged basis during this campaign. The AirMetrics samplers were operated with $PM_{2.5}$ impactor separation heads for approximately the first half of the field study and were then switched to PM_{10} heads for the remaining portion of the study. Each AirMetrics sampler was fitted with a conditioned, pre-weighted Teflon filter and operated at approximately five liters per minute for a time-controlled 23-hour period. Following sampling, the filters were recovered, conditioned, and reweighed for filter catch and ultimate determination of each location's $PM_{2.5}$ and PM_{10} mass concentrations. Weather stations (Davis) were located at the trailer and the lidar to record meteorological parameters (wind speed, direction, temperature, etc.) Wind speed profiles and turbulence dynamics were also collected on the central tower using 3D sonic anemometers.

In the described experiment, the lidar trailer was located at approximately 650 m west of the central tower (see fig 3.1). This location allowed 3D volume measurements of particulate emissions from the three barns from a single observation point. Azimuth and elevation scan speeds for these data were 0.05-0.2 degrees per second.

2) *Emission Sources*: Examples of vertical, horizontal, and stationary (time series) lidar observations are shown in figs. 4.2 and 4.3. These images show the intensity

of the logarithmic range-normalized power (see (3.5)) with background radiation removed.

Occasional traffic along the two unpaved roads bordering the swine production facility caused extensive fugitive dust that traveled over and around the swine facility. These events were observed and classified in the lidar retrieval development. While originally considered a nuisance, the difference in physical composition and size range provides a good demonstration of the lidar's capabilities. The particulate emission from the barns is clearly distinguished from the fugitive road dust due to separation of these events in space and time.

The particulate emissions from barns were localized at a distance of ~650 m from the lidar, while fugitive dust clouds appeared at a variety of ranges (~1550 m in fig. 4.2(a)). The vertical scan in fig. 4.2(a) was measured at a still wind condition so that both the fugitive dust cloud and the particulate emission are spatially localized around their respective emission sources. They are shown expanding upwards to ~120 m due to

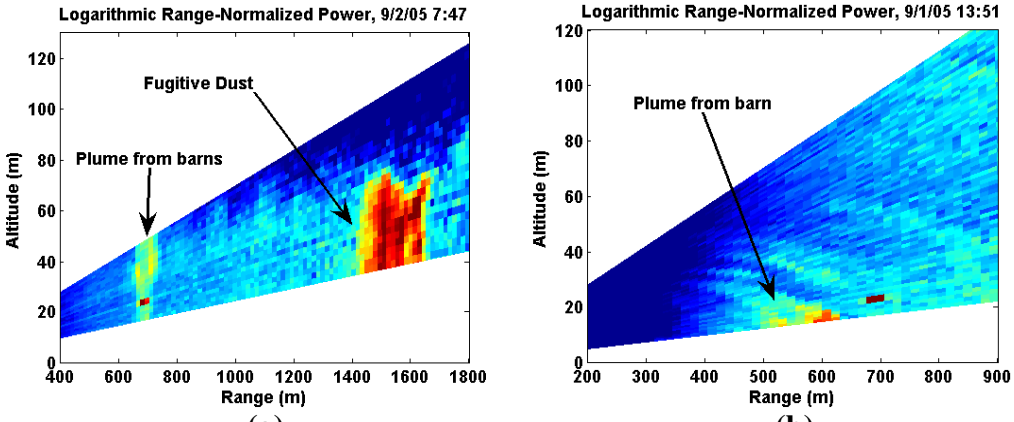

(a) **(b)**

Fig. 4.2: Vertical scan examples.

convective turbulence. Figure 4.2(b) shows the facility plume under west wind condition. The particulate cloud is blown toward the lidar and does not rise higher than ~40 m. The horizontal scan in fig 4.3(a) was taken at a height of 16 m under south wind conditions with speed of ~3 m/sec. It shows the horizontal dispersion and intermittent character of particulate emission from the barns (schematically indicated in this image). The time series in fig. 4.3(b) was measured under south wind conditions when fugitive dust was blown from the south road, which was parallel to the line of lidar range measurements. The lower density plume at a range of ~650 m represents particulate emission between swine barns measured at a height of ~8.5 m in a close proximity to the OPC sensor mounted on the tower.

Due to the spatial and temporal separation of the fugitive dust and swine facility emissions in the return lidar signal, these events can be evaluated separately and their optical and physical properties can be extracted from a single lidar scan. For all cases, the signals from fugitive dust were about an order of magnitude stronger than those from the barn emissions. The barn emissions only slightly exceeded lidar returns from the

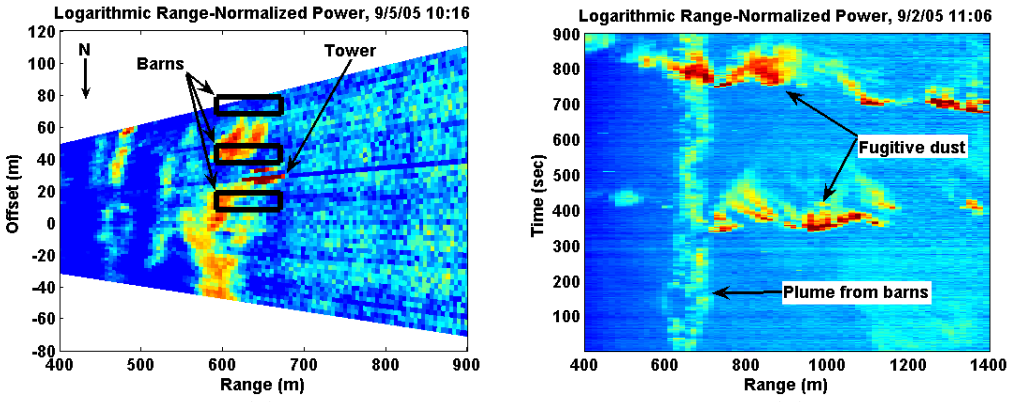

(a) **(b)**

Fig 4.3: Horizontal scan and time series examples.

background aerosols in the surrounding air on some occasions. The retrieval procedure described in the previous chapter was tested on both cases.

B. *Experimental Results*

1) *Swine Particulate Emissions*: Side-by-side comparison of mass concentrations PM_{10} retrieved from the lidar data with in situ measurements by OPC sensors are shown in fig. 4.4(b). This time series represents the first 100 seconds of the time series presented in fig. 4.4(a).

The portion of the lidar beam near the middle of the central tower measured the emission plume, while the lidar path on the far side of the particulate cloud was assumed to measure the background. In many cases the particulate emissions from the swine facility exceed the background aerosol loading only slightly. Lidar returns are still sensitive to these small variations, which can be easily spotted due to their spatial localization within the lidar signal, as illustrated by fig. 4.3(b). The OPC sensors provide continuous point measurements and are not spatially located within the exact plume

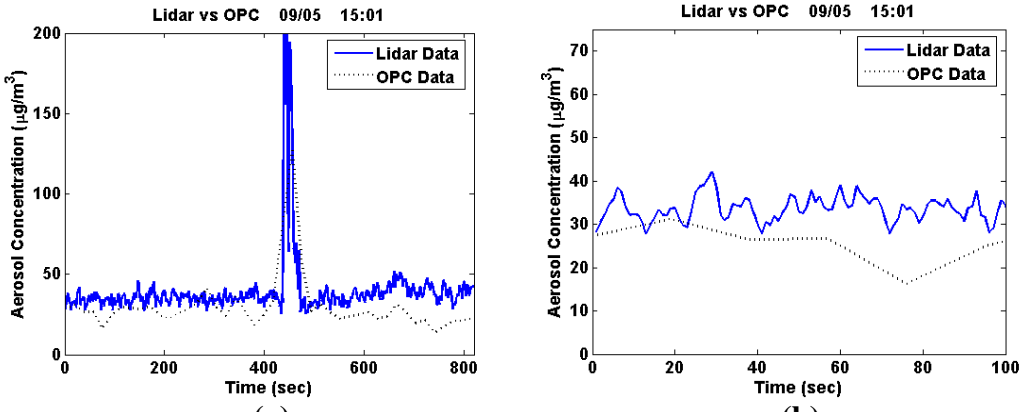

Fig. 4.4: Lidar and OPC comparison.

maximum, so that background aerosols and particulate emission can be distinguished temporally by changes in the intensity of the signal. Comparison of the OPC data measured between barns and far away from barns, where it is assumed only background aerosol is present, shows that particulate emission counts only slightly exceed the level of natural variability of the background aerosol loading. In this case it is difficult to extract exact information on the particulate physical parameters from the OPC data.

The ability of the lidar system and algorithm to retrieve particulate concentration at a level comparable with the natural variability of background aerosols is demonstrated in fig 4.5. Particulate mass concentrations PM_{10} and $PM_{2.5}$ are retrieved from the lidar time series measurements taken at the middle of the tower. It is seen that aerosol was emitting from the barns with a periodicity of 5-10 seconds. During these observations, the lidar accumulation time was set to 1 second, and that was enough to resolve the periodic nature of particulate emission. The accumulation time of the OPC instruments is 20 seconds, which is insufficient to sample these periodic events. This contributed to the

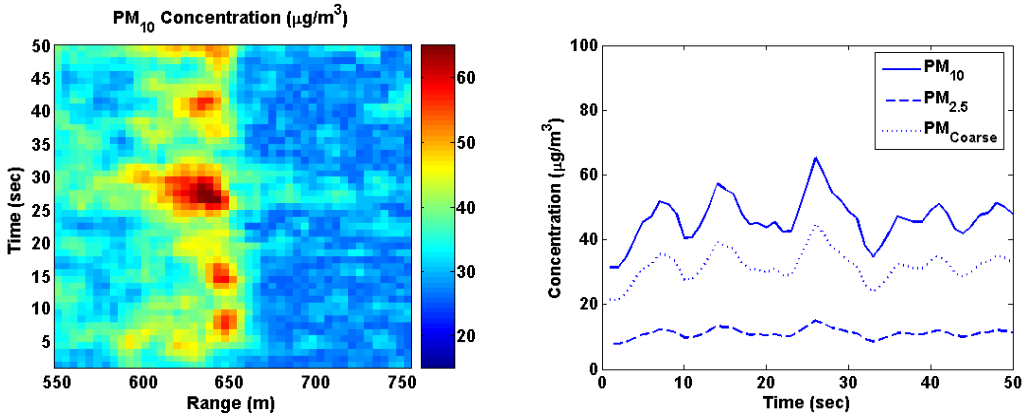

Fig. 4.5: PM concentration time-series comparison.

inability of the OPC instruments to resolve clearly the particulate emissions and background aerosols.

The concentration fields measured from the upwind and downwind sides of the swine production facility are demonstrated in fig. 4.6. These are vertical scans measured from the south and north sides of the farm under south wind conditions. The data are presented as PM_{10} mass concentration field on the upwind and downwind sides of the facility. The integrated difference of these profiles can be multiplied by the wind speed to estimate total particulate flux leaving the production facility.

2) *Fugitive Dust*: The versatility of the retrieval algorithm is demonstrated by retrievals of PM concentration during fugitive dust events. The results one such retrieval is demonstrated in fig. 4.7. Optical coefficients for the three laser wavelengths are shown in fig. 4.7(a) as a function of range. The results converting these measurements to PM concentrations are shown in fig. 4.7(b). Under south wind conditions the dust cloud was moving perpendicular to the lidar field of view so that at each lidar range the cloud has

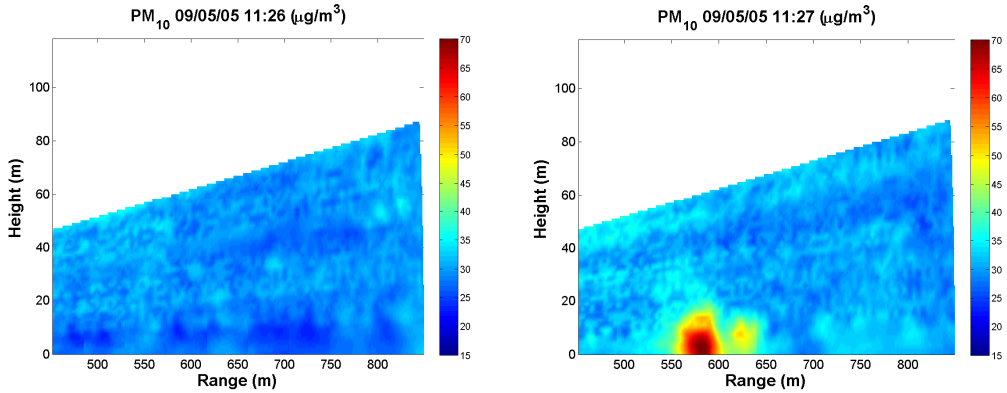

(a) **(b)**

Fig. 4.6: Upwind vs. downwind profile comparison.

moved practically the same distance from the road.

A comparison of measurements of fugitive dust by both the lidar and OPC instruments can be seen in fig. 4.4(a). Both measurements represent a time series of particulate emission measured simultaneously at the middle of the central tower. There is a large peak in the data approximately 450 seconds into the scan. This concentration peak represents a fugitive dust event and the base signal is mostly due to the background and pollutant aerosols. The values for fugitive dust concentration measured by the lidar are both in qualitative agreement with coincident OPC measurements.

C. *Field Calibration*

For agricultural emission and flux measurements, the absolute value of retrieval quantities became a major factor in the evaluation of lidar retrievals. Validation data for this experiment were derived from AirMetric portable PM_{10} and $PM_{2.5}$ samplers placed at different locations around the hog farm. These samplers represent an EPA-approved

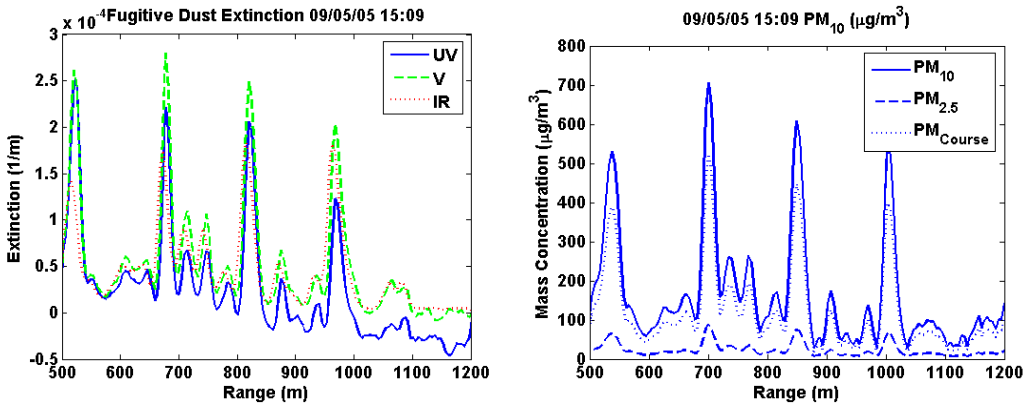

(a) **(b)**

Fig. 4.7: Fugitive dust optical and physical properties.

method of measuring particulate mass concentrations and appear to be the best source of calibration data. The mass concentrations of particulate emission acquired with samplers at different locations around the facility were analyzed, and the main results are shown in fig. 4.8. The background, non-barn influenced PM_{10} and $PM_{2.5}$ concentrations were found to average around 38.7 ± 5.4 μg/m^3 and 13.2 ± 3.8 μg/m^3, respectively. Plume values measured between barns, at the central tower, and at the sensor trailer (under downwind conditions) varied within wide ranges, 38-75 μg/m^3 and 11-18 μg/m^3 with average values 49.4 ± 8.3 μg/m^3 and 14.7 ± 3.3 μg/m^3 of PM_{10} and $PM_{2.5}$ mass concentrations, respectively. The uncertainty values given here and illustrated in fig. 4.8 represent the confidence interval, derived from the internal variability of the dataset.

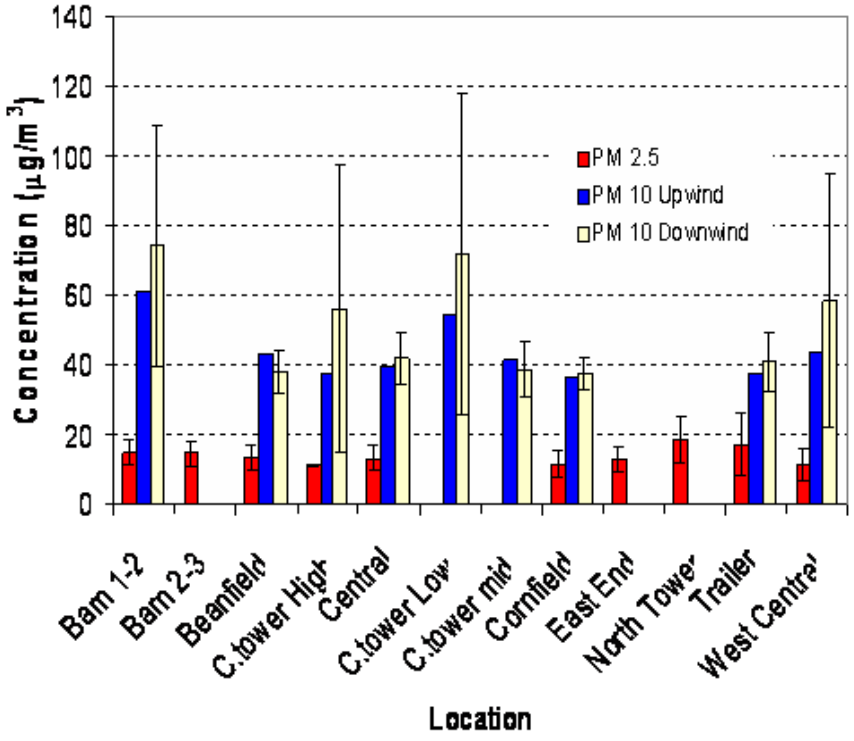

Fig. 4.8: Airmetric sampler PM results.

While the AirMetric samplers measure integrated particulate mass over a 23-hour period, the OPC instruments allow for continuous measurement of particle counts. Data from the AMS are fused with the OPC data to produce particle size distributions continuous over all size ranges. The particle size distribution is used to calculate total particulate volume, which when combined with sampler measurements yields particulate density. In addition, by applying Mie theory to the OPC and AMS data, atmospheric optical parameters are calculated at each location with 20 sec. temporal resolution. These parameters include the backscatter coefficients β_b and the lidar ratios of both the background and the pollutant aerosols.

The correlation of aerosol data acquired by optical instruments (OPC and lidar) and aerodynamic instruments such as PM samplers is complicated by the complexity and uncertainties in aerosol chemical composition, the irregularity of the shape of the particles of which the aerosols are composed, and differences between particle optical and aerodynamic properties.

To avoid the complexity of this correlation, a simple calibration procedure is adopted. OPC data collocated with Airmetric samplers were averaged over the Airmetric sampling time of 23 hours at each location and were converted to effective total particulate volume. The effective density of background and pollutant particles was calculated by dividing the effective total particulate volume by the mass values measured by the samplers. These data were then averaged over several days in multiple locations, and a mean value of the effective density q* was calculated for both background and pollutant aerosols.

In this way, a density value of $q^* = 2.1 \pm 0.44$ g/cm^3 was estimated, which agrees

well with water-soluble aerosol density (q= 1.8 g/cm^3) from atmospheric aerosol databases. This density value is used as a calibration parameter to convert particle size distributions measured by the OPC and lidar sensors to the mass concentration units measured by the EPA approved samplers. A comparison of calibrated lidar data with calibration in situ data was previously illustrated in fig. 4.4.

CHAPTER 5

ERROR ANALYSIS AND DISCUSSION

A. *Sources of Error*

The derivation of particulate concentration from lidar photon counts involves several retrieval steps and sources of data. The combination of these sources of error can compound each other and make it difficult to estimate the expected error in the retrieval process. Knowledge of error is an essential part of any measurement campaign. A comprehensive analysis of the error in the Aglite algorithm has not yet been performed and will be required for future development.

1) *Background Radiation*: The most apparent source of error is the optical noise, described in (3.1), from background radiation and sensor noise. For a range-normalized signal, this noise has a variance described by (3.4), which depends on the level of background radiation, measurement integration time, and measurement range.

The effect of this error is two-fold. First, this noise can drown out small spatial and temporal variations in background aerosol.. This error, however, does not have a DC component and does not bias the data. Secondly, at farther ranges the lidar signal becomes so weak in comparison to the background noise that retrieval of any kind becomes impossible. This was illustrated previously in fig. 3.2, where the visible channel becomes so noisy that it is irretrievable after 600 m. The relative strength of the background noise to the lidar signal determines this upper limit on retrieval distance.

2) *Algorithm Error*: Another source of error is introduced by the Klett retrieval

method itself. The Klett method, described by (3.16), has a pole, which means the solution is unstable for measurements beyond the reference point. Furthermore, this solution does not take error into account, but rather is simply a solution to the lidar differential equation.

Currently, the retrieval of backscatter and the retrieval of particulate concentration are two separate steps, optical parameter retrieval and aerosol size distribution retrieval. In the first step, the aerosol is described only by the relatively simple lidar ratio, while in the second step, the aerosol is described by all of the parameters of the particle size distribution. A potentially better retrieval method would be to combine these two steps into one retrieval step that minimized the error between the measured and estimated data, while simultaneously imposing all known constraints on the solution. Additionally, such an algorithm would also be able to provide error estimates simultaneously with retrievals.

3) *Reference Point Error*: Another source of error, which is potentially more harmful to the retrieval process than either background noise or algorithm error, is measurement calibration error. The Klett retrieval method requires a reference point, where the atmospheric backscatter value is known. This reference point calibrates the rest of the points in the measurement. In general terms, the Klett retrieval returns the backscatter values at all the remaining points in the measurement by finding the relative value at every lidar measurement point as compared to the lidar reference point and returning a backscatter value that has the same ratio to the reference backscatter value.

Error in either the lidar reference point or in the reference backscatter value will cause proportional error in all lidar measurement points. This introduces a bias into the entire measurement. The effect of reference point error is shown in fig 5.1, where the

reference point value is perturbed by 20%.

Lidar reference point noise can be caused by background radiation noise, but it can also result from reference point estimation error. An absolute reference point exists only if a point in the lidar beam path is co-located with in situ instruments. If a lidar measurement lacks a reference point, one can be created using a reference point from another measurement. The relationship between the reference points from different measurements is shown here in terms of the logarithmic range-corrected signal.

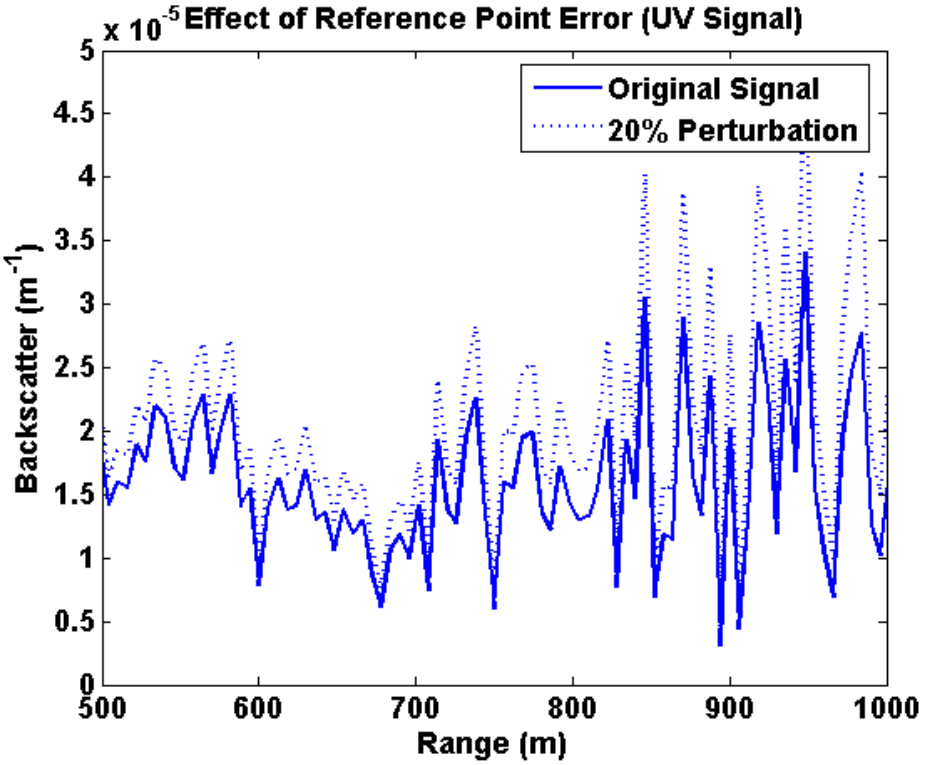

Fig. 5.1: Reference point error.

$$S_0^\beta - S_0^\alpha = \ln\left|\frac{\beta_0^\beta}{\beta_0^\alpha}\right| - 2\int_0^{z0}\sigma^\beta(z') - \sigma^\alpha(z')\partial z' \tag{5.1}$$

$$\beta_0^\beta = \beta_0^\alpha \exp\left(S_0^\beta - S_0^\alpha\right)\exp\left(2\int_0^{z0}\sigma^\beta(z') - \sigma^\alpha(z')\partial z'\right)$$

$$\beta_0^\beta \approx \beta_0^\alpha \exp\left(S_0^\beta - S_0^\alpha\right)$$

The terms S_0^α and S_0^β represent the range-corrected signal values at the reference range for two different measurements.

If the difference in the extinction integrals for the two measurements is negligible, then the backscatter value at the new reference point can be approximated. This error, however, introduces an error into the reference backscatter value, which will in turn propagate to the rest of the measurement.

4) *In situ Instrument Error*: Error in values from the in situ instruments also leads to retrieval error. In situ instrument error can be caused by either error in particle size distribution estimation, as described by (2.12), or by inaccurate assumptions of particulate index of refraction and shape.

Error in particle size distribution parameters will lead to error in retrieving particulate concentration. Error in the reference point backscatter and in the lidar ratio will lead to inaccurate backscatter retrievals. In situ instrument error can be caused by either in situ instrument error or by local spatial backscatter variability in the atmosphere around the in situ instruments.

5) *Range Error*: There are two sources of range error that are inherent in the lidar design itself, the geometric form factor and measurement error due to photon counting. The geometric form factor causes distortion to the lidar signal, blocking out the signal as

it approaches the lidar. The geometric form factor is difficult to reliably measure and correct, as was previously illustrated in fig. 3.2(d). This adds increasing error as the signal approaches the lidar.

The photon counting problem occurs at far distances. Normally, the background radiation swamps out the lidar signal, making retrievals past a certain point impossible. Under night-time conditions however, the background is sufficiently small that the usable range of the lidar increases. Under these conditions, a new source of error limits the range of the lidar. The lidar signal is measured in photon-counts, and as range increases, the received signal eventually falls to such low levels that the noise from the discrete nature of the signal becomes significant.

B. *Logistical Requirements*

There are several requirements that must be satisfied during a measurement campaign. These requirements allow the lidar retrievals to be successful and reliable.

First of all, the lidar must be placed appropriately. The lidar must have sufficient stand-off distance from the target source, but at the same time be as close as possible. Experience has shown that the geometric form factor limits measurements to no closer than 500 m, and reliable retrievals are only possible at ranges closer than 1500 m.

Secondly, in situ instruments must be placed appropriately to measure the background aerosols and to provide reference point values for the lidar retrieval. These instruments should be placed at least 500 m and no more than 1500 m from the lidar, and preferably in a location where they will not be affected by the target aerosol. In situ instruments should also be placed near the target source in order to measure the target

aerosol particle size distribution parameters. This is not as firm a requirement, as pollutant backscatter can be estimated using (3.17).

Lastly, the lidar should be placed so as to minimize the physical obstacles between the lidar and target, such as trees and power lines. Solid objects in a signal either partially or fully obscure measurements taken beyond them. Additionally, the signal from a physical object can be difficult to differentiate from the aerosol signal that one is attempting to measure. Physical objects can be removed using a median filter, but the remaining residue still contributes error to the result.

C. *Future Directions*

At the time of the writing of this thesis, the Aglite system has already been deployed on four campaigns, and several more are being planned. It is projected that the Aglite system will be used on many campaigns a year and that there will be little time for data processing between campaigns.

Currently it takes about four months to process a data set from a campaign. This clearly needs to be sped up. The retrieval algorithm needs to be implemented as a relatively fast stand-alone computer program that can be run in the field. This program needs to give accurate and reliable results.

The current form of the algorithm is a series of Matlab scripts that require considerable user input and management. It is anticipated that the algorithm will be implemented as a single stand-alone application in C++ with a simple user interface. Additionally, an error study for the algorithm needs to be performed so that error estimates for particulate concentration retrievals can be given.

Finally, it is hoped that an algorithm with superior accuracy can be developed. As mentioned previously, the current algorithm consists of two retrieval steps that were not developed from an error-minimization perspective. It is hoped that a faster algorithm can be developed that performs the retrievals more accurately in a single step.

REFERENCES

[1] S. J. Hoff, K. C. Hornbuckle, P. S. Thorne, D. S. Bundy, and P. T. O'Shaughnessy, “Emissions and community exposures from CAFOs”, Iowa State University and The University of Iowa Study Group - Report, p. 221, 2002.

[2] T. Shibata, M. Kobuchi, and M. Maeda, "Measurements of density and temperature profiles in the middle atmosphere with a XeF lidar," *Applied Optics*, vol. 25, pp. 685-688, 1986.

[3] L. Menut, C. Flamant, J. Pelon, and P. Flamant, "Urban boundary-layer height determination from lidar measurements over the Paris area," *Applied Optics*, vol. 38, pp. 945-954, 1999.

[4] D. I. Cooper, W. E. Eichinger, J. Archuleta, L. Hipps, J. Kao, M. Y. Leclerc, C. M. Neale, and J. Prueger, "Spatial source-area analysis of three-dimensional moisture fields form lidar, eddy covariance, and a footprint model," *Agricultural and Forest Meteorology*, vol. 114, pp. 213-234, 2003.

[5] V. A. Kovalev and W. E. Eichinger, *Elastic Lidar: Theory, Practice, and Analysis Methods*, Hoboken, NJ: John Wiley and Sons, Inc., 2004.

[6] B. A. Holmen, W. E. Eichinger, and R. G. Flocchini, “Application of Elastic Lidar to PM_{10} Emissions from Agricultural Nonpoint Sources,” *Environmental Science & Technology,* vol. 32, pp. 3068-3076, 1998.

[7] S. S. Cornelsen, "Electronics design of the aglite-lidar instrument," M.S. thesis. Utah State University, Logan, 2005.

[8] S. W. Dho, Y. J. Park, and H. J. Kong, "Experimental determination of a geometric form factor in a lidar equation for an inhomogeneous atmosphere," *Applied Optics*, vol. 36, pp. 6009-6010, 1997.

[9] C. D. Cooper and F. C. Alley, *Air Pollution Control: A Design Approach*, Prospect Heights, IL: Waveland Press, 1997.

[10] W. C. Hinds, *Aerosol Technology: Properties, Behavior, and Measurement of Airborne Particles*, New York: John Wiley and Sons, Inc., 1999.

[11] J. D. Klett, “Lidar inversion with variable backscatter/extinction ratios,” *Applied Optics*, vol. 24, pp. 1638-1643, 1985.

[12] G. J. Kunz, "Inversion of lidar signals with the slope method," *Applied Optics*, vol. 32, pp. 3249-3256, 1993.

[13] F. G. Fernald, B. M. Herman, and J. A. Reagan, "Determination of aerosol height distributions by lidar," *Journal of Applied Meteorology*, vol. 11, pp. 482-489, 1972.

[14] R. M. Measures, *Laser Remote Sensing: Fundamentals and Applications*, New York: John Wiley and Sons, Inc., 1984.

[15] D. Muller, U. Wandinger, and A. Ansmann, "Microphysical particle parameters from extinction and backscatter lidar data by inversion with regularization: theory," *Applied Optics*, vol. 38, pp. 2346-2357, 1999.

[16] *Handbook of Geophysics and the Space Environment*, Air Force Geophysics Laboratory, United States Air Force, 1985.

[17] C. Böckmann, "Hybrid regularization method for the ill-posed inversion of multiwavelength lidar data in the retrieval of aerosol size distributions," *Applied Optics*, vol. 38, pp. 2346-2357, 1999.

[18] S. Twomey, *Introduction to the Mathematics of Inversion in Remote Sensing and Indirect Measurements*, New York: Elsevier, 1977.

[19] M. Del Guasta, M. Morandi, L. Stefanutti, B. Stein, and J. P. Wolf, "Derivation of Mount Pinatubo stratospheric aerosol mean size distribution by means of a multiwavelength lidar," *Applied Optics,* vol. 33, pp. 5690-5697, 1994.